

Ref #1

General comments:

This manuscript presents a generally well written study on a new MLT ozone data set retrieved from O2 IR A-band airglow emission measurements with the IR imager on the Odin satellite. The calibration of the IRI measurements is described, as is the retrieval approach and a first comparison with independent satellite measurements. The study presents an interesting and relevant contribution to the field and should eventually be published. I ask the authors to address the following comments, many of which are really minor.

I have two general comments:

1. The section on the calibration of the IRI measurements should be more specific and detailed. I guess this paper will be THE paper on the calibration of these measurements and will be used as a reference for future papers. The description is not detailed enough to understand the details and to reproduce the individual steps. I'm not asking for every little detail to be explained, but more information on the vague parts should be provided (see also the specific comments below).

A more detailed description on calibration will be included in another paper, which is aimed for submission in several months by Saskatoon authors.

2. The agreement of the IRI O3 retrievals with some of the other data sets is not very good or rather poor at some altitudes, latitudes and/or time of the year. The authors offer different explanations for these differences, but issues with the photochemical model are not discussed. I think this is an obvious candidate to investigate. I'm not asking for new analyses etc. but suggest mentioning that the model may be an issue here and may / will be tested in a future study. In my opinion the data sets (IRI and co-located SMR measurements are a unique opportunity to test and improve the photochemical model.

The issue with the uncertainty in the photochemical model is mentioned in the introduction section as well as in the ozone retrieval section. But this will be re-emphasized again in the result/discussion section in the updated version of the manuscript. Indeed, IRI and SMR measurements are a unique opportunity to test and improve the photochemical model in a future study. In the course of this study we noted some instability in the mesospheric part of the SMR profiles. While the average profiles are fine in order to properly tune the model individual profiles of good quality are needed. We therefore reserve this for a later. We would like to thank referee #1 for the valuable input to help us improve the manuscript.

Specific comments: Title: "OSIRIS observation" → "OSIRIS observations"? **Corrected in the revised version.**

Line 12: "19 years-long mission" → "19-year mission" ? **Corrected in the revised version.**

Line 38: "affect the inferred ozone distribution, especially whose lifetime is comparable to the transport timescales." Something is missing / wrong here. Please correct. **Corrected in the revised version as "Furthermore, the photochemical timescales of the airglow species critically affect the inferred ozone distribution, especially species whose lifetime is comparable to the transport timescales."**

Line 54: "Degenstein et al. (2005b)" I suggest changing the order of the papers in the reference list such that Degenstein et al. (2005a) is cited first. **Degenstein et al. (2005a) is cited in line 26 before Degenstein et al. (2005b) is cited in line 54.**

Line 64: “sample .. have been processed.” -> “sample .. has been processed.” [Corrected in the revised version.](#)

Line 70: “we also include MIPAS and ACE-FTS ozone profiles, measurements retrieved from other satellites”

This is only a really minor thing, but “measurements retrieved” sounds somewhat strange. I tend to associate “measurements” with the initial radiance spectra measurements. Perhaps you could write, e.g. “.. ozone profiles, i.e. data sets retrieved from measurements with instruments on other satellites”. I leave it up to you to decide, whether you want to change this or not. [Corrected in the revised version.](#)

Line 83: “emissions with” -> “emissions with a” ? [Corrected in the revised version.](#)

Line 91: “dark current and electronic offset” -> “dark current and electronic offset correction” [Corrected in the revised version.](#)

Line 93: “version of (Bourassa, 2003).” -> “version of Bourassa (2003).”, i.e. wrong cite command used. [Corrected in the revised version.](#)

Line 116: “The fitting process is a periodized” Please explain what “periodized” means in this context. It is unclear to me. [The fitting process is split into temporal chunks that span several calibration periods of the IR instrument \(which are roughly every 50 orbits for the bulk of the mission\). In this way, small changes in the calibration parameters can be tracked as the satellite instrument ages. This will be clarified in the upcoming paper](#)

Line 131: “The in-flight curves closely resemble the pre-flight curves with notable differences towards the edges of the arrays.” It would be interesting to show this comparison, because this paper will probably serve as a description of the calibration process also to be used for future studies. [This will be clarified in the upcoming paper.](#)

Line 141: “The shape of the stray light is then extrapolated to lower tangent altitudes” Please describe, how this is done. There are many different ways to extrapolate data. [This is a big section with a lot of discussion, thus it will be left in the upcoming paper.](#)

Line 148: “or photons per second from a unit area” from a unit area? I think it’s photons passing through a unit area, right? [Corrected in the revised version.](#)

Same line: “The usual per nm wavelength dependence of the radiance” This would then be “spectral radiance”. The quantity with your units is simply “radiance” [The usual unit of spectral radiance is not used in this formulation as the spectral information is effectively lost by integration of the signal across the passband. The radiance or brightness units are then photons per second.](#)

Line 162: “The final reported error also incorporates the error in the pixel electronics offset” How is the final error determined based on the individual error components? This should be explained in more detail. [This will be clarified in the upcoming paper](#)

Figure 1, left panel, x-axis label: “Radiance” Units missing. [Corrected in the revised version.](#)

Line 187: “The value of phi is relatively insensitive to the emission temperature.” Can this be quantified? If you have tested that it is relatively insensitive to T, you should be able to easily provide a rough quantitative estimate. [In the updated retrieval procedure, we have implemented the temperature dependent fraction of the optical filter overlapping the emission band, i.e. the value of](#)

phi, being temperature dependent, based on the temperature at the tangent point. The description is added to the revised version of the manuscript.

Caption, Figure 2: “Every two rows” -> “Every second row”? Corrected in the revised version.

Line 181: space missing in “B-band(688nm)” Corrected in the revised version.

Line 300: “are only sensitive below 90km or below.” ? Corrected in the revised version.

Line 330: “Eq.9” -> “Eq. 9” Corrected in the revised version.

Caption, Figure 6: “Every two rows” -> “Every second row”? Corrected in the revised version.

Caption, Figure 7: “scaled with their corresponding a priori profiles.” -> “divided by the corresponding a priori profiles.” This figure is deleted. However, the updated/added figures which show the relative error are written 'error size relative to the individual a priori profiles' in the captions.

Line 347: “the 20 years data” -> “20 year data set” Corrected in the revised version as 'the 20-year-dataset'.

Line 386: “the thermal emission line of ozone” Line? It’s many, many lines, right? No, it is a single line

Line 388: “Van Der A” -> “Van der A” Corrected in the revised version

Line 406: “SMR ozone measures from” -> “SMR provides/measures ozone from” Corrected in the revised version

Figure 8, IRI data: Why is O₃ negative over such an extended altitude range? It would be good to discuss potential reasons in more detail. What about problems with the photochemical model? Please also mention, whether the VERs are also already negative in these regions. VERs are not negative but very low for this region. The main reason for such an extended region of negative values mainly comes from the fact that the photochemical equilibrium assumption is used in the model, while this assumption is hard to be considered valid in that region. On top of that, the model includes the contribution from O₂ ground state to produce O₂(1aDelta), therefore the inversion tries to force O₃ to be very low, even negative, to overcompensate the low VERs being observed. In short, the steady state assumption will underestimate O₃ concentration when this assumption is not valid. We have added this discussion in the revised manuscript, as well as a novel approach to address this issue in an updated procedure for reprocessing IRI O₃ data (see the newly added Sect. 2.3.3.)

Line 425: “every 20th orbits .. have” -> “every 20th orbit .. has” Corrected in the revised version

Line 343: “and therefore blanked out in Fig. 9.” Please check grammar of this sentence. Something is missing here. (perhaps Line 434) The section and figure have been rewritten in the revised version therefore this comment is no longer relevant.

Line 437: “MIPAS observes a deeper trough in the winter hemisphere as in IRI and SMR data, but a relatively even distribution in the MLT region.” I can’t really see that in the figure. What does “deeper” refer to here? The ozone values or altitude? This is not clear. The section and figures have been rewritten in the revised version therefore this comment is no longer relevant.

Lines 441 following: The authors discuss differences in SZA as a cause for the differences between the different datasets. This is certainly a possible reason, at least for part of the differences. But are the differences between the data sets consistent with the diurnal variation of O₃ and the different

SZAs of the measurement shown in Fig. 10? This could be easily addressed qualitatively. This figure and the discussions about differences in SZA sampling are no longer in the revised manuscript, as the reprocessed IRI data show significantly closer to MIPAS zonal mean data compared to the version before.

Figure 11, left panel: x-axis label is wrong -> " cm^{-3} " This figure is no longer in the revised manuscript.

Line 454 following: It should also be mentioned that the differences can be significantly larger at other latitudes. We have expanded the difference figure to include all overlapping latitude bins (see Fig. 14 in the revised version), excluding ACE-FTS as referee #2 provided the reason not to include this dataset in the paper.

Line 474: "Overall, IRI agrees very well with SMR" Looking at Figures 9 and 12, I think this statement is not justified. Relative differences between the two data sets reach very large values, right? With the newly added Fig. 14 in the revised version, it is shown that the updated IRI data has generally 20-50% positive bias compared to SMR and MIPAS.

Line 477 following: "The differences between IRI, ACE-FTS and MIPAS in Fig.12 may be explained .." There may also be issues with the photochemical model used to retrieve O₃. I think this should be explicitly mentioned. The dataset should be used in future studies to attempt to improve the photochemical model used. We acknowledge this comment. This is emphasized in the revised version.

Figure 12: I suggest that negative values are more clearly indicated (e.g. in black). The current depiction makes it difficult to identify negative values. After the IRI data being reprocessed with the modification in measurement uncertainty scaling with the equilibrium index, the negative values in such plots are mostly replaced by a priori value with low measurement response. Data with low measurement response and low equilibrium index are filtered out before making an averaging profile.

Table A2: "ACE-FTS tmospheric" Thank you for pointing out the typo. However, ACE-FTS will be removed from this paper for ozone comparison as pointed out by referee #2.

Ref #2

A general reply to Ref #2:

We do not intend the main focus of the paper to be a complete and comprehensive validation study of the new data set of mesospheric O₃. Rather in this paper we focus on presenting the retrieval technique, and the utility of the OSIRIS limb emission profiles as a sample data set for this type of high resolution mesospheric O₃ data product. This primary goal is mentioned in the end of Sect.1 and beginning of Sect.3. Indeed, if the entire ~20 year Odin-OSIRIS data is processed, it would comprise a very valuable data set as the reviewer acknowledges. The processing of the entire 20 year OSIRIS data set with the new instrument corrections and using the inversion technique to the Level 2 product is a substantial computational undertaking and must be addressed in future work beyond this first paper.

We would like to thank to referee #2 by raising several important discussion questions that have helped us to improve the manuscript and the data processing method, namely the equilibrium assumption issue accompanying 1.27 μm emission being the proxy of O₃, and the absorption corrections on the VER retrieval.

The manuscript does fall into the scope of AMT. It deals with a potential new data set of daytime mesospheric O₃ and it is therefore very important. Eventually it can be sufficiently sound to be posted in its discussion forum but, in my opinion, not in its current form. I think it needs a substantial revision before it can be posted.

I would recommend to the authors the following actions:

The first part of the paper is well written, clear and well focused. This section, however, still requires some actions as:

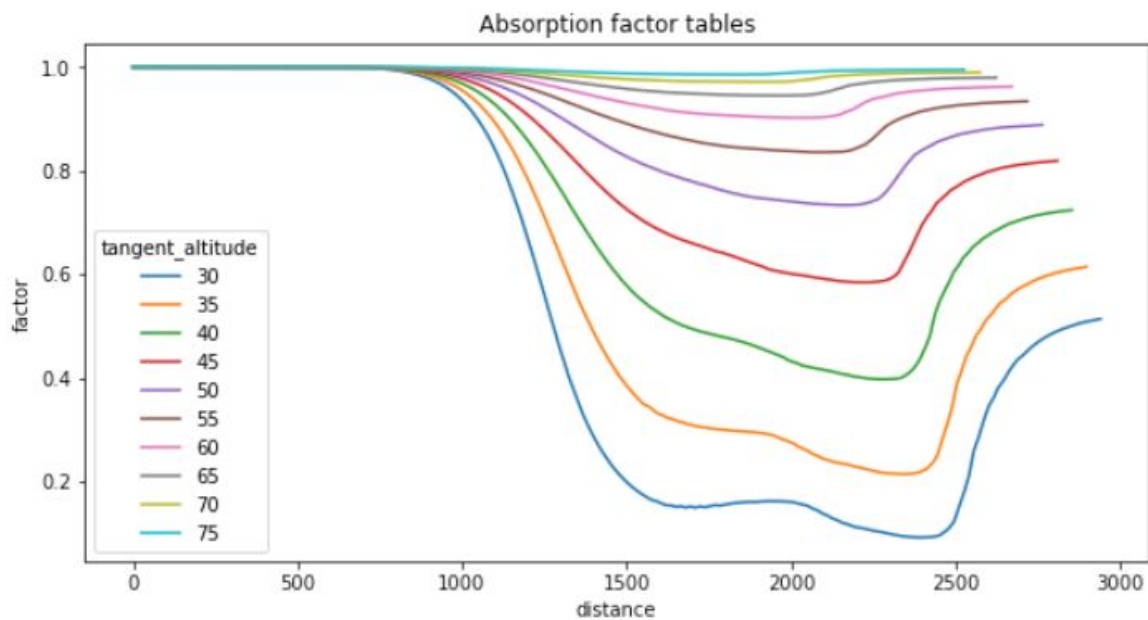
1) Include a Table listing all error sources and their estimated values. It is true that in order to verify if the estimated systematic errors are plausible (for example that of the stray-light, particularly near 80 km when the atmospheric signal is very small but radiance for the bright region below might be important) one needs to perform a thorough validation. Hence, I propose to present that in the second part of the paper (see below).

We agree that a table summarising all error sources and their estimated values would improve the paper. However, quantification some of the error sources can only be done after more data being processed, or require a comprehensive modelling study such as in Zhu et al. (2007), thus it will be left to the future validation study. We have however provided a table of possible error sources, quantifying those that can be quantified and estimation others at the end of Sect. 2.

2) To include a proper radiative transfer (i.e., do not assume the optically thin approach) for the 60-70 km region. Although the authors cite Degenstein (1999) (a Thesis work) as a support for the validity of this approach in that region, Mlynczak et al. (2007) state that "Below 70 km absorption of the O₂(1D) emission by O₂ itself begins to become important and the weak-line retrieval approach becomes invalid."

I suggest that a) include full RT below 70 km, b) limit the data to 70 km, or c) estimate (quantitatively) the errors of that approach in the 60-70 km region.

We acknowledge this limitation. We have reprocessed the VER retrieval by introducing an absorption correction factor to address this issue. The correction factor is calculated based on the tangent pressure (see the revised Sect. 2.2). The changes on the resulting VERs are less than 10% in the 60-70 km region, as shown in the figure below.



The figure shows the correction factor along the tangent path compared to the optically thin case along the tangent path. Colours correspond to different tangent heights of the paths in the unit of km. As can be seen from the red line representing line-of-sight tangent of 60km, the absorption would result in approximately 10% underestimation for the band intensity for emission near the tangent point. Furthermore, this factor is formatted in a pressure grid and applied to the retrieval scheme according to the pressure level at the tangent point.

3) If I have understood correctly, the 1.27 μm channel has not been calibrated in flight. It is just assumed that it behaves as other inflight-calibrated channels. I have not seen any error associated with this (lack of) calibration in the manuscript.

We acknowledge this comment. Odin carries no optical calibration sources. As mentioned in Sect. 2.1.4, the absolute calibration relies on the pre-launch value, and for the 1.53 μm channel this has been confirmed in flight as indicated in the paper. As at this point, assessment of the uncertainty due to the in-flight changes in the absolute calibration is difficult. The long term stability of this channel will however need to be assessed when the full 20 years of data is processed. Thus the characterisation of this type of error source will be addressed in the future study. However, we have included this in the error

source list as suggested in point 1) in the revised manuscript.

2nd part. Section 3.

This section is a mixture of a kind of a soft (descriptive, not rigorous) validation exercise together with some partial description of the behaviour of O₃, incomplete from my point of view. In my view, none of the two aspects are shown with sufficiently sound scientific treatment.

We would again like to emphasise that we do not intend this paper to be a comprehensive validation study of a new data product. We acknowledge the reviewer's point that the comparative statements regarding the measurements by the various instruments are somewhat soft, yet we believe these are useful comparisons (not validation) to show the fidelity of the retrieval technique. We agree with the reviewer that a comprehensive validation that uses the entire Odin-OSIRIS data set would indeed be valuable and we hope to be able to address this in a future paper.

For example, the current validation is only descriptive, a kind of hand-waving comparison, side by side figures, e.g., not showing differences, no co-location criteria has been used (or at least not mentioned). Sentences like "The differences between IRI, ACE-FTS and MIPAS in Fig.12 may be explained by their sampling at different SZA and the underlying assumptions in their retrieval techniques." are very vague and little informative. If sampling is a cause, the differences should be looked at by restricting it. Etc.

We agree that this comparison is descriptive. We mainly intend to demonstrate an Odin internal comparison of their co-incident profiles, as they are based on different physical measurement techniques and overlapping. Yet, these side-by-side figures show that the ozone profiles from three independent Odin-borne instruments complement each other well. Showing the differences between the coincident profiles would not be particularly informative in this case, due to their limited overlapping altitude range.

Regarding the comparison of zonal mean monthly average distribution with other instruments, an updated difference plot is provided in Fig. 14 including several latitude bands in order to make it more complete. We would like to point out again that, as stated in Sect. 3, only a test sample of 5% of all the measurements collected during a one-year period has been processed for this study. This information has been also added to the introduction section in the revised version.

About the second aspect, the study is mainly descriptive and based on partial datasets and considering the O₃ number density instead of the O₃ vmr. Sentences like: "Thus such a monthly mean profile should be treated with caution since it may not necessarily well represent the spatial and temporal distribution of daytime ozone." again adds little information. If it does not represent the distribution, why then show it? The study on the "Monthly mean ozone" is based on 1 month of one year and of O₃ density. I would suggest the authors to refer to other similar studies (e.g. Lopez-Puertas et al. 2018).

We use number density mainly as it is the natural unit for the IRI measurements. Moreover, for SMR O₃ at higher altitudes, the lines are mainly Doppler broadened rather than pressure broadened, thus the natural unit is closer to number density rather than VMR. Of course, IRI can be converted to VMR, by introducing external data such as MSIS, as shown in a small portion of Fig. 11. As Smith et al. 2003 mentioned, the different background density to

derive VMR may introduce additional uncertainty between O3 profiles from different instruments, we would like to avoid introducing external data. We have addressed this issue in the revised version.

Fortunately, thanks to the updated scheme of ozone retrieval, the zonal mean monthly average ozone demonstrated in Fig. 12 and Fig. 13 agree much better with MIPAS than those in the previous version of the manuscript. We agree that the study is descriptive in regard to the behaviour of O3, indeed based on what we can tell from the limited amount of data we have at the moment. We intended to confirm that IRI data is able to reproduce a general pattern of the O3 distribution in the MLT.

My recommendation for this section 3, would be to focus on a thorough, rigorous validation (following the standard guidelines, see some more comments below) and leave aside from this paper the kind of characterisation of O3 features. Maybe the authors would like to consider future papers as, e.g. the overall OSIRIS O3 data sets, or tackle comprehensive works, including or not other datasets, as seasonal/latitudinal variations, or local time and annual variations, etc.

We want to emphasise again that a comprehensive validation study is not the focus of this paper. We acknowledge that a rigorous validation study is indeed valuable for a future study, after the ~20 years data will be processed. Section 3 is intended to provide a first-hand comparison in order to demonstrate the fidelity of the retrieval technique described in Sect. 2, which is our primary focus in this paper. We have described our purpose more clearly in the revised version.

Recommendations on validation:

1) It should be based on collocated data and, whenever possible, the same physical conditions, e.g., based on a coincidence criteria of time, spatial (latitude, longitude) and local time.

This issue can be addressed providing that more IRI data are processed and a sufficient amount of coincidence profiles between MIPAS and IRI are found. However, as already explained above, this can not be done at this stage.

2) Compare the appropriate instruments. That is, there is no altitude overlap of IRI wrt SO. Hence I see no reason for including SO data.

After the reprocessing of the IRI data with a correction on absorption, data can reach as low as 40km (50km after the last 10 grids were removed to avoid edge effect coming from the retrieval), thus IRI and OS has at least 10km of overlapping. Moreover, it is the first time to demonstrate how these three ozone data sets from Odin complement each other so well, despite their intrinsically different underlying physics in terms of measurement techniques. This also shows for the broader scientific community how Odin can cover a large part of the atmosphere using its different instruments. Thus, we do not want to completely remove the OS data set from this study, particularly Fig. 11.

- About MIPAS data, I suggest the author include a more appropriate reference, e.g., Lopez-Puertas et al. (2018). MIPAS middle atmosphere data ranges from ~20 km (not 5 km, Table 1) up to ~100 km. BTW, I believe the authors have used only DAYTIME MIPAS data (not stated explicitly in the manuscript). Mention which pressure/temperature is used (MSIS?, MIPAS?) to calculate O3 density.

We acknowledge the reference. MIPAS night time ozone is screened out as described in line 442. To calculate the density, we use pressure and temperature measured by MIPAS. We have provided this information in the revised version.

- I would be inclined to not include ACE data. O3 shows a large diurnal variation in the mesosphere and ACE is always measuring at the terminator. Hence it is difficult to distinguish systematic differences inherent to the instruments from those due to the solar illumination. BTW, the authors should state early in the paper that the 1.27 μm emission has a radiative lifetime of approximately 75 min and does not provide a representative measure of ozone until 2–3 h after sunrise (Mlynczak et al., 2013). Has this fact been taken into account in the current comparison? This fact automatically should avoid to compare to ACE sunrise occultations.

We agree that, for ACE data, it is difficult to distinguish the differences due the solar illumination from those inherent to the instrument. Thus we have removed ACE data for this study.

Regarding the long radiative lifetime of the 1.27 μm emission, we have added this information early in the revised version of the manuscript. In addition, we address this issue in an updated inversion process of ozone by increasing the uncertainty matrix of the VER, based on an 'equilibrium index',

$$\text{Index} = 1 - \exp(-t/\tau),$$

where τ is the total lifetime ($\tau = 1/(A+Q)$) of the 1.27 μm emission, being the combination of the emission lifetime ($1/A$) and the quenching lifetime ($1/Q$) at a given altitude. This index indicates how far to the photochemical equilibrium state at a given altitude and time after the local sunrise. The detailed descriptions are provided in the newly added Sect. 2.3.3. In short, the effect of the newly introduced 'equilibrium index' in the O3 retrieval will suppress the underestimation of O3 where the steady state assumption is invalid, and thus these regions will be filtered out by low measurement responses before making comparisons with other ozone datasets.

- I am really missing a validation against SABER. In particular the O3 derived from the O2 1.27 μm channel. This is an instrument that uses the same technique and would therefore be very valuable.

Indeed it will be very valuable to compare SABER 1.27 O3 to IRI O3 in a future study, when the full data set will be processed and we will be able to carry out a validation study rigorously based on the comparison of coincident profiles. However, measurements from SABER drift in local time, unlike all other instruments included in this paper. For this reason, we have decided not to include SABER in this first study.

3) Quantify the differences (of the co-located data) for the different seasons/latitudes/altitudes. That is, as Fig. 11, but including more altitudes/seasons and enough years of retrievals to make the statistic significant.

A new figure including differences of more latitudes is added, see Fig. 14. The comparisons between IRI and OS, SMR are always coincident. Based on the available IRI one-year-data set, it is difficult to have a statistically significant number of coincident profiles with MIPAS. As mentioned earlier, the focus of this study is on the retrieval technique. Processing a statistically significant amount of data for several years would require substantial computation undertaking and thus this should be left for future studies.

About the 2nd part, a description of the O3 characteristics should be presented in a different paper and I would recommend the authors to please cite other previous recent works about this.

Other minor points:

In general several many figures are very small, particularly those with several panels, e.g. Fig. 3, 5, 9 and 11

It is revised in the new version of manuscript.

Fig. 3 Could you show the solar local time?

Solar local time for Odin is relatively constant (6h,18h). Instead, we have added the time after the local sunrise axis in the figure.

a typo: earth -> Earth

It is revised in the new version of manuscript.

Retrieval of daytime mesospheric ozone using OSIRIS ~~observation~~ observations of $O_2(a^1\Delta_g)$ emission

Anqi Li¹, Chris Roth², Kristell Pérot¹, Ole Martin Christensen¹, Adam Bourassa², Doug Degenstein², and Donal Murtagh¹

¹Chalmers university of technology, Department of Space, Earth and Environment, Gothenburg, Sweden

²Institute of Space and Atmospheric Studies, University of Saskatchewan, Saskatoon, Canada

Correspondence: Anqi Li (anqi.li@chalmers.se)

Abstract. Improving knowledge of the ozone global distributions in the mesosphere-lower thermosphere (MLT) is a crucial step in understanding the behaviour of the middle atmosphere. However, the ~~ozone concentration~~ concentration of ozone under sunlit conditions in the MLT is often so low that its measurement requires instruments with very high sensitivity. Fortunately, the bright oxygen airglow can serve as a proxy to retrieve the daytime ozone density indirectly, due to the strong connection to ozone photolysis in the Hartley band. The OSIRIS IR imager (hereafter IRI), one of the instruments on the Odin satellite, routinely measures the oxygen infrared atmospheric band (IRA band) at 1.27 μm . In this paper, we will primarily focus on the detailed description of the ~~detailed steps~~ steps done for retrieving the calibrated IRA band limb radiance, the volume emission rate of $O_2(a^1\Delta_g)$ and, finally, the ozone number density. This retrieval technique is applied to a one-year-sample ~~IRI dataset~~ from the IRI data set. The resulting product is a completely new ozone ~~dataset with very high~~ data set with very tight along-track ~~resolution~~ sampling distance (<20 km). The performance of the retrieval technique is demonstrated by a comparison of ~~the~~ coincident ozone measurements from other instruments aboard the same spacecraft, as well as zonal mean and monthly average comparisons between ~~OS, SMR, MIPAS and ACE-FTS. The consistency of this IRI ozone dataset implies that such a~~ Odin-OSIRIS (both spectrograph and IRI), Odin-SMR and Envisat-MIPAS. We find that IRI appears to have a positive bias of up to 25% below 75 km, and up to 50% in some regions above. However, the IRI ozone data set is consistent with the compared data set about the overall atmospheric distribution of ozone. We attribute these differences in uncertainty in the IRI calibration as well as uncertainties in the photochemical constants. This implies that the retrieval technique can be further applied to all the measurements made throughout the ~~19-years-long~~ 19-year mission, leading to a new, long-term, high resolution ~~dataset~~ ozone data set in the middle atmosphere.

Copyright statement. Copyright is retained by the authors

20 1 Introduction

The distribution of ozone plays a key role in the middle atmosphere, ~~such that it~~. It can influence the radiative budget, thus affecting temperature structures and ~~the~~ dynamic flow patterns (Brasseur and Solomon, 2005). As such, attention has been drawn to the observations of ozone over the past decades. The existence of the stratospheric ozone layer, resulting from the absorption in the Herzberg continuum, was proposed early last century and subsequently confirmed (Chapman, 1930). Near the
25 mesopause region, a secondary ozone layer, which is the result of radiation absorption in the Schumann-Runge continuum, was later detected (Hays and Roble, 1973). More recently, the existence of a tertiary ozone maximum was discovered by multiple measurements both from ground-based and satellite instruments (e.g., Marsh et al., 2001). The tertiary ozone maximum only occurs in winter, in the high-latitude middle mesosphere. The mechanism behind it is mainly due to a decrease in atomic oxygen losses involving the odd-hydrogen species near the polar night terminator. However, the detailed picture of the tertiary
30 ozone maximum is not yet fully explained because of the complexities in both the chemical composition and the dynamics of the mesosphere and lower thermosphere (MLT) (e.g., Hartogh et al., 2004; Degenstein et al., 2005a; Sofieva et al., 2014; Smith et al., 2018).

Satellite observations provide us with valuable knowledge on the behaviour of atmospheric ozone. In the MLT region, various measurement techniques are employed to monitor the ozone distribution. For instance, there are observations of ozone
35 absorption by using solar or stellar occultation (e.g. HALOE, ACE-FTS, SOFIE, GOMOS) (all acronyms are given in Table A2), of emission from thermally excited ozone (e.g. SABER at 9.6 μm , MIPAS, SMR) and of airglow emission (SME, SABER and SCIAMACHY at 1.27 μm , OSIRIS at 762 nm). Smith et al. (2013) have shown comparisons of ozone concentrations in the MLT region resulting from most of the above mentioned techniques. They have concluded from coincident profile comparisons that different measurement principles agree with each other reasonably well (better than 20% for the instruments
40 considered here). However, they emphasise that the differences in local time sampling among the measurements ~~affected~~ impact the inferred global distribution in the MLT, for instance, the vertical structure and seasonal variations of ozone. ~~Other than~~ Additionally, differences in measurement principle ~~and~~, sampling schedules, uncertainties in the calibration and band-passes of the instrument, and inaccurate pointing knowledge may also ~~contribute~~ be factors contributing to the difference between these ozone observations. ~~Furthermore,~~

For ozone measurements based on inference assuming photochemical equilibrium the photochemical timescales of the air-
45 glow species can critically affect the inferred ozone distribution, especially ~~whose lifetime is the species whose lifetime are~~ comparable to the transport timescales. The 1.27 μm oxygen emission has a photochemical lifetime of about 74 minutes ~~which~~ can affect the measurements (Newman et al., 2000) which can influence the retrieved ozone quantity in two ways. One is the effect of ~~transport~~ advective and diffusive transport of the relevant species, and the other ~~can be~~ is the delay in reaching
50 quasi-photochemical equilibrium after sunrise. Zhu et al. (2007) have evaluated the uncertainties in daytime ozone retrieved from 1.27 μm emission due to the effect of tidal waves and the photochemical steady state assumption, by using a dynamical-photochemical coupled airglow model.

In this study, we will focus on the retrieval of the ozone data collected by instruments aboard the Odin satellite, particularly primarily the OSIRIS IR imager (hereafter IRI). The Odin satellite is orbiting the Earth around 15 times per day since 2001 and is still fully functional (Murtagh et al., 2002). SMR (Submillimeterwave-SubMillimeterwave Radiometer) and OSIRIS (Optical Spectrograph and Infrared Imaging System) are the two main components on Odin. Both of them instruments measure various species closely related to the middle atmospheric ozone chemistry by observing the Earth's limb. Furthermore, OSIRIS includes OSIRIS, in fact, consists of two optically independent instruments: the optical spectrograph (hereafter OS) and the infrared imager. IRI has three vertical imagers. Two of them measure the oxygen infrared atmospheric band (IRA band) emissions centred at 1.27 μm , and the third one measures the OH Meinel band emission centred at 1.53 μm . A more detailed description of IRI can be found in Sect. 2.1 as well as in Llewellyn et al. (2004). Data collected by one of the oxygen IRA band imagers have been studied by Degenstein et al. (2004) to demonstrate a tomographic retrieval technique to derive airglow volume emission rate and its comparison to non-tomographic retrieved volume emission rate. Degenstein et al. (2005b) showed the potential of the IRI observations for estimating ozone depletion during a Solar Proton Event. The observations of oxygen IRA band and the OH Meinel band together were used to study the mesospheric tertiary ozone peak by Degenstein et al. (2005a). To our knowledge, there is no further investigation which deals with the dataset-data set from the IRI instrument.

Our primary objective in this paper is to revisit the oxygen airglow measurements obtained from the IRI at 1.27 μm and demonstrate a retrieval scheme used to derive the volume emission rate as well as the ozone concentration in the MLT region based on Bayesian estimation. In addition, we address the issue of the validity of the photochemical equilibrium assumption by using a novel technique in the ozone retrieval. This ozone product will be a completely new dataset-data set from the Odin mission and is complementary to the already existing ozone measurements since the signal strength in the MLT region during daytime is often too low for the other instruments. In addition, this IRI ozone product has about 70 times higher along-track sampling rate than the other ozone products thanks to the imaging technique.

To illustrate the performance of the retrieval technique, a small but representative sample (every 20th orbit) of the IRI measurements collected from November 2007 to October 2008 have-has been processed. Our secondary focus is to demonstrate the fidelity of the resulting new IRI ozone product, by a side-by-side comparison of monthly mean zonally averaged distribution with other independent ozone measurements, namely OS, SMR, ~~MIPAS and ACE-FTS and MIPAS~~ ozone products. However, we would like to emphasise that this paper is not intended to be a full validation study. IRI, OS and SMR observe at the same geographical location and time because they are on board the same platform, thus the bias due to the different sampling schedules mentioned in Smith et al. (2013) is negligible. However, ~~due to their differences in altitude coverage to give a more complete picture of the IRI data set,~~ we also include MIPAS ~~and ACE-FTS ozone profiles, measurements retrieved from other satellites, ozone profiles~~ in our comparison ~~to give a more complete picture of the global nature of the agreement. Their demonstrated consistency (although this reintroduces the issues with local time sampling). Even though biases are found (see Sect. 3.4), we find that the data set can reproduce the general seasonal and latitudinal pattern of the ozone distribution, which~~ indicates that the presented IRI ozone retrieval scheme can be applied to the whole 19 years of the mission to date, opening new opportunities to perform further scientific studies.

~~Also, we want to highlight that it is novel to illustrate how the~~ We also for the first time show results from all three ozone data sets ~~from Odin collected by the Odin satellite, illustrating how they~~ complement each other ~~so well well. And agree,~~ despite their intrinsically different underlying physical bases in terms of measurement techniques. ~~For a broader scientific community,~~ we demonstrate that Odinean cover a large part of the atmosphere using its different instruments And thus, by adding Ozone retrieved from the IRI instrument to Odin's repertoire we expand the possibility for future studies using data from this venerable research satellite.

2 Theory and implementation

In this section, we will discuss the necessary steps to derive the calibrated limb radiance (in Sect. 2.1), then the volume emission rate of the oxygen IRA band (in Sect. 2.2) and, finally, the ozone number density profiles (in Sect. 2.3). The theoretical background, as well as the implementation details can be found in the corresponding subsections.

2.1 Level 1 data – calibrated limb radiance data

The IRI instrument measures the oxygen IRA band with 10 μm wide filters ~~entered-centred~~ at 1.273 μm and 1.263 μm (channels 2 and 3, respectively, in OSIRIS nomenclature) and the OH Meinel emissions with a 40 μm wide filter ~~entered-centred~~ at 1.530 μm (channel 1) (Degenstein et al., 2004). All three of the single-lens IR imagers consist of a linear array of 128 InGaAs photodiodes (pixels). Each array is split into two sections: a masked off, permanently dark portion of approximately twenty pixels used for calibration, and the remaining pixels used for data collection. The optical portion of the IRI instrument was designed such that the angular spacing between photodiodes results in approximately 1 km separation between the tangent altitudes of the look vectors. Each image of the IRI system consists of a measurement of each of the 128 pixels. Images are taken approximately every two seconds with a one-second duration exposure time.

Like any photodetection system, the IRI must be calibrated to remove instrument dependent effects from the measurement and convert the digital count into calibrated radiance. This calibration process occurs in four steps: (1) dark current and electronic offset correction, (2) relative calibration of the pixel gain, (3) removal of stray light, and (4) absolute calibration. The calibration process applied to the IRI data used in this work is an updated version of (~~Bourassa, 2003~~) Bourassa (2003). A short description of each step follows.

In this paper, we will only look at data taken from channel 3 centred at 1.263 μm .

2.1.1 Dark Current and Electronic Offset

Each of the 128 pixels in the linear array of photodiodes has a unique temperature dependent dark current characteristic. The signal is referred to as “dark current” as it is thermally generated and present regardless of whether or not the photodiode is subject to light (photons). As is typical of semiconductor systems this small number of thermally generated electron-hole pairs have a Poisson distribution and follow the Shockley equation.

The electron-hole diffusion current and recombination current are proportional to

$$e^{-E_g/k_B T} \tag{1}$$

and

120 $e^{-E_g/2k_B T}$, (2)

respectively, where E_g is the band gap energy, T , the temperature, and k_B , Boltzmann's constant.

In practice, each pixel's unwanted thermal signal can be characterised by a single exponential term of the form

$$\gamma_i e^{\beta_i/T}, \tag{3}$$

for each pixel i in the array, where γ and β are parameters found by implementing least-squares curve fitting to the data.

125 In addition to the removal of the dark current, two sources of electronic offset must also be characterised and removed from the measurements. The first is a relatively time-invariant electronic offset that is unique to each pixel. By adding a parameter that characterises each pixel's unique electronic offset to the above equation, a three-parameter fit is used for each pixel

$$\alpha_i + \gamma_i e^{\beta_i/T} \tag{4}$$

130 where α is the offset parameter. The second form of electronic offset is the same for each pixel, but varies randomly with each image due to noise in the electronics. This is handled separately from the three-parameter fit.

Calibration data for the IRI instrument, where an optical shutter is closed to block out incoming light, is used to compute the three parameters (for each pixel) at regular intervals throughout the mission. The fitting process is a periodized, least-squares optimisation.

135 By applying the parameters found using the calibration data to the data collection portion of the mission where the optical shutter is open, the dark current and the pixel dependent electronic offset are removed from the raw data. The image dependent electronic offset can then be determined, and subtracted off, using the permanently dark masked off pixels.

In short, this step calibrates each photodiode's measurement to zero (within measurement error consistent with shot noise) when not exposed to light.

2.1.2 Relative Calibration of the Pixels

140 In this step, referred to as the relative calibration or pixel "flat fielding", each pixel's output is normalised so that a uniform input brightness on each pixel results in the same digital counts. Prior to launch, the instrument was subjected to a calibrated Lambertian light source to determine these parameters, but early mission data revealed that the pre-launch relative calibration curves were no longer accurate.

145 To perform an in-flight relative calibration of the pixels, the mesospheric night-time airglow layer was used in place of a calibrated Lambertian source. As the IRI instrument scans up and down through this layer, comparisons are made between neighbouring pixels as they pass through the same layer to derive this relative gain factor for each pixel. Although the airglow

layer is not constant in brightness, the statistical impact of this variation becomes negligible as the number of intercomparisons becomes large. The relative calibration algorithm was applied to every applicable night time orbit. The resulting data was averaged to create an in-flight relative calibration curve that is applied to the IRI data. The in-flight curves closely resemble the pre-flight curves with notable differences towards the edges of the arrays.

2.1.3 Stray Light Removal

It is evident from the IRI data that off-axis light from the sunlit Earth is incident on the IR detectors due to scattering and diffraction. An in-depth modelling of the IRI optical system was performed by Ivanov (2000). This work and Bourassa (2003) finds that during the sunlit portions of the orbit, the measured signal is the sum of the atmospheric brightness and a large unwanted stray light signal from the off-axis Earth below.

To remove the stray light, its shape is first characterised using data where the amount of real incident light is negligible. This occurs when the pixel look direction tangent points are over 100 km. The shape of the stray light is then extrapolated to lower tangent altitudes and the magnitude of stray light for any image is assumed to be proportional to the average brightness of the pixels over 100 km. As the number of pixels over 100 km changes from image to image due to the nodding nature of the Odin spacecraft, the quality of the stray light removal process changes; becoming less accurate when fewer pixels are present over 100 km. This decrease in accuracy is accounted for in the error estimate of the data related to the stray light removal process.

2.1.4 Absolute Calibration

Finally, the data is multiplied by a factor to convert the digital number measurement of the read-out electronics to a measurement of calibrated radiance reported in $\frac{\text{photons}}{\text{s}\cdot\text{cm}^2\cdot\text{sterad}}$, or photons per second ~~from~~ [passing through](#) a unit area within a unit solid angle. The usual per nm wavelength dependence of the radiance, common in remote sensing observations of a spectrum, it is not used in this formulation as the measurement is an integral over the infrared band filter.

The absolute calibration value used to convert the data from digital counts to brightness was determined through calibration sessions pre-launch. Post-launch the calibration value for the 1.53 μm channel was checked by comparing it to a standard single Rayleigh scattering model of the atmosphere, which showed that the pre-launch value was still applicable. As there is no equivalent simple atmospheric model to test against the 1.27 μm , and there has been no evidence to conclude otherwise, the assumption is that the absolute calibration values for channels 2 and 3 are also still applicable.

2.1.5 Calibration Error

Throughout each step in the calibration process, uncertainties are calculated so that the uncertainty values given with the final calibrated data are meaningful and accurate.

To begin with, the error in the measured digital number of read-out electronics is a combination of two sources: the shot noise of the detector and the random error due to the fact that the number of photons incident on the pixel array follows a Poisson distribution (which is negligibly small for all but the brightest of scenes.)

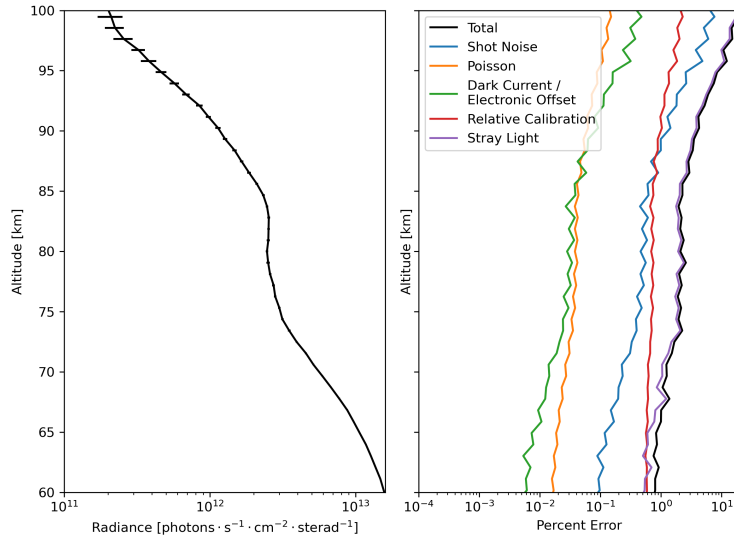


Figure 1. Left: A sample daytime exposure of IRI radiance data (image 1250 of orbit 37400, see Fig. 4 for reference). Right: The corresponding total error and error contributions.

The final reported error also incorporates the error in the pixel electronics offset, and is the combination of the errors determined through the various calibration steps: the error in pixel electronics offset and thermal characteristics, the error in
 180 the relative calibration curve, and finally the error in the stray light calibration table.

Figure 1 shows the radiance profile of a sample IRI exposure. The vertical axis is tangent height of the pixel's look direction rather than pixel number. For daytime exposures, a total error between 1-10% is typical with the stray light error as the largest contributing factor.

Figure 2 shows a sample orbit of IRI limb radiance and its relative error size.

185 2.2 Retrieval of $O_2(a^1\Delta_g)$ airglow volume emission rate

Once we have obtained the calibrated limb radiance, the next quantity to derive is the volume emission rate, since the volume emission rate of photons emitted in the oxygen infrared atmospheric band is directly related to the number density of $O_2(a^1\Delta_g)$ by its radiative lifetime (i.e. Einstein A coefficient). In this paper, only daytime measurements are considered since we rely on a photochemical scheme, described in Sect. 2.3, to derive the ozone number density. However, IRI also collects high quality
 190 data in the night part of the orbits (~~not shown~~) ~~which will be~~ which is valuable for other studies.

~~We will use a linearized scheme to retrieve volume emission rate profiles. The retrieval problem becomes linear if we assume that the majority of the signal originates from the tangent layer emissions. However, this means that data measured at tangent altitudes lower than a certain level should not be included for the analysis as the measured signal becomes dominated by properties of other atmospheric layers due to absorption and scattering processes. Degenstein (1999) has indicated that~~

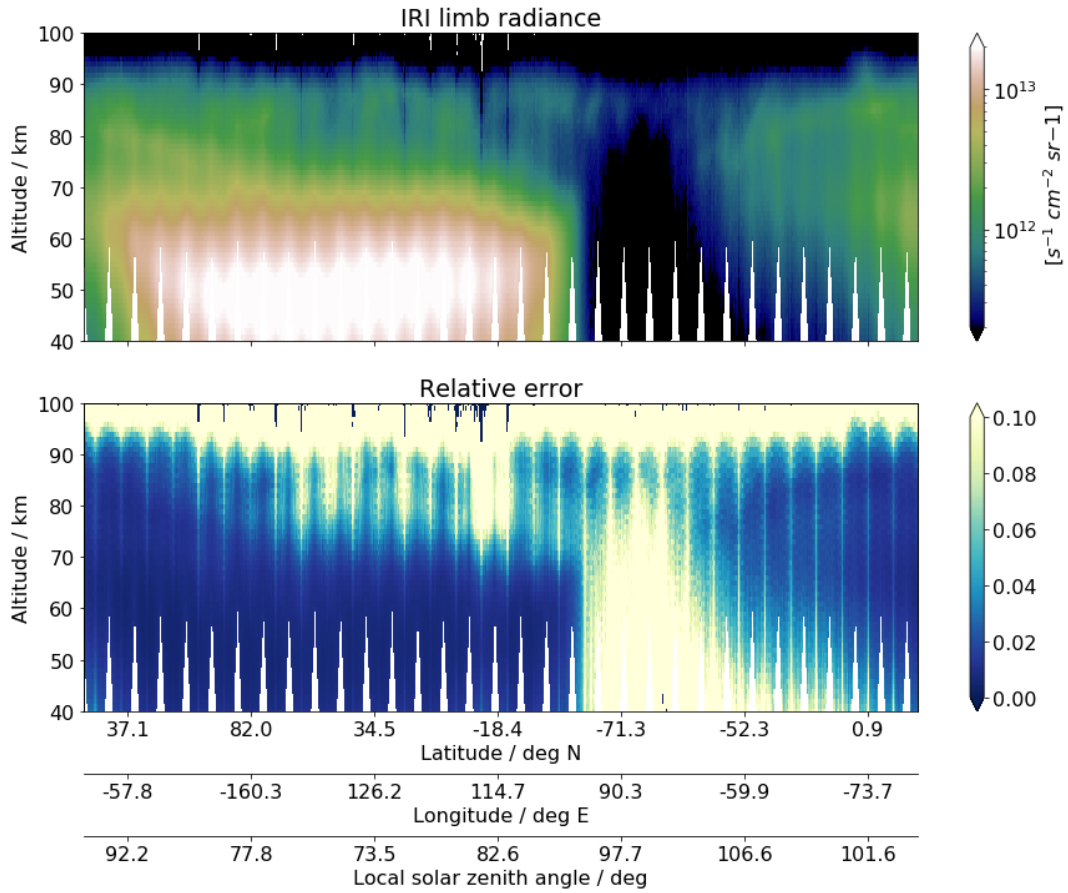


Figure 2. Left: A sample daytime exposure An example of IRIS-IRI limb radiance data and its relative error size for one orbit collected on 2008-03-30, from 22:21:09 to 23:09:13 (image 1250 of orbit 37400 number 38720). Right: The corresponding total error, as a function of geographical location and error contribution stangent altitude. Local solar zenith angle is also shown in the horizontal axis.

195 self-absorption of the oxygen IRA band becomes significant when line-of-sight tangent is lower than 60. Hence we use this as a lower bound of limb radiance data selection. An upper bound of 100 km line-of-sight tangent height is chosen due to the weak emission signal above the airglow layer.

The IR imager measures the limb radiance R which is described by the radiative transfer equation

$$R = \frac{\phi}{4\pi} \int V(s) e^{-\tau(s)} ds, \quad (5)$$

200 where $V(s)$ is the volume emission rate over the full band at location s along the line-of-sight of the instrument. ϕ is the ‘filter factor’ defined as the overlap between the instrument filter and the oxygen IRA band emission lines, and $e^{-\tau(s)}$ is the transmissivity between the emission source at s and the instrument along the line-of-sight. As previously explained, we assume no self-absorption, $e^{-\tau(s)}$ therefore simply becomes unity. The value of ϕ is equal to 0.72 for the channel considered in this

paper-estimated from a simple spectral calculation using the HITRAN (Gordon et al., 2017) catalogue for the emission line
 205 strengths. ~~The value of ϕ is relatively insensitive to the emission temperature. Thus the~~, and it changes with the atmospheric
 temperature at the tangent point.

In this paper, we will use a linearised scheme to retrieve volume emission rate profiles. The retrieval problem becomes
 linear if we assume that the majority of the signal originates from the tangent layer emissions. However, absorption and
 scattering processes may become important where the atmospheric layer that the line-of-sight penetrates is optically thick.
 210 In the case of the oxygen IRA band emission, Degenstein (1999) has indicated that self-absorption is important to consider
 when line-of-sight tangent is lower than 60 km. In order to account for the issue of absorption, we pre-compute a table of
 the absorption factors $e^{-\tau(s)}$ as a function of the line-of-sight along the tangent path, and scale the measured limb radiance
 accordingly. The absorption coefficients are taken from HITRAN and MSIS ((Picone et al., 2002)) is used for temperature and
 pressure. The relationship between the measured limb radiance and volume emission rate ~~becomes purely linear and can can~~
 215 ~~then~~ be expressed as

$$y_i = \sum_j k_{ij} x_j + \epsilon_i = \frac{4\pi R_i}{\phi}, \quad (6)$$

where y_i is the column emission rate for the full oxygen IRA band as would be measured by the pixel i (which is proportional
 to R_i), x_j the volume emission rate at the atmospheric layer j , k_{ij} the path length of the line-of-sight i through the atmospheric
 layer j weighted by the absorption factor and ϵ_i the measurement errors. In matrix notation, the relationship can thus be
 220 expressed as

$$\mathbf{y} = \mathbf{K}\mathbf{x} + \boldsymbol{\epsilon}, \quad (7)$$

where \mathbf{y} is also termed the measurement vector, \mathbf{K} the weighting function, or Jacobian matrix and \mathbf{x} the state vector.

In this paper, the optimal estimation method (OEM), also known as the maximum a posteriori (MAP) method (Rodgers,
 2000), is employed to invert the above equation. By constraining the inversion using the uncertainties of both the measured
 225 quantity and the a priori knowledge, the estimated profile of the volume emission rate can be expressed as

$$\hat{\mathbf{x}} = \mathbf{x}_a + \mathbf{G}(\mathbf{y} - \mathbf{K}\mathbf{x}_a), \quad (8)$$

where \mathbf{x}_a denotes the a priori profile of volume emission rate, and \mathbf{G} the gain matrix, which is equal to:

$$\mathbf{G} = (\mathbf{K}^T \mathbf{S}_e^{-1} \mathbf{K} + \mathbf{S}_a^{-1})^{-1} \mathbf{K}^T \mathbf{S}_e^{-1}, \quad (9)$$

where \mathbf{S}_e and \mathbf{S}_a are the error covariance matrices describing the uncertainties of the measurement \mathbf{y} and of the a priori profile
 230 \mathbf{x}_a , respectively.

In our implementation, \mathbf{x}_a is the $\text{O}_2(\text{a}^1\Delta_g)$ volume emission rate profile calculated by the photochemical model (see Sect.
 2.3) by inputting the ozone profile from a climatology. This climatology was derived from the data presented by the Canadian
 Centre for Climate Modelling and Analysis known as the CMAM model ¹ and evaluated for different latitudes, months and

¹CMAM data is downloaded at <http://climate-modelling.canada.ca/climatemodeldata/cmam/cmam30/>

local solar times for the tangent points of the IRI measurements. The covariance matrix of the a priori follows

$$235 \quad S_a(i, j) = \sigma_a(i) \sigma_a(j) \exp(|i - j| \frac{dz}{h}) \quad (10)$$

where σ_a is set to be $0.75x_a$ and $dz/h = 1/5$. The off-diagonal elements act as a regularization on the estimation to prevent oscillations. S_e has diagonal elements equal to the square of the uncertainty of each pixel (i.e. the calibration error described in Sect. 2.1). All off-diagonal elements for S_e are set to zero, that is assuming no correlation between errors for different pixels in the limb radiance measurements. The retrieval grid covers altitudes from 50~~10~~ km to 130 km with 1 km spacing. ~~Thus we have~~
 240 ~~a~~To select the limb radiance measurement, a lower bound of 40 km and an upper bound of 100 km line-of-sight tangent height are chosen. Thus, a 30 km margin for both the lower and upper bounds ,respectively, in order to minimize~~minimise~~ any edge effect in the inversion process.

The vertical resolution of the retrieved data can be represented by the averaging kernel (AVK) matrix,

$$\mathbf{A} \equiv \frac{\partial \hat{\mathbf{x}}}{\partial \mathbf{x}} = \mathbf{G}\mathbf{K} \quad (11)$$

245 which maps the changes from the true state \mathbf{x} to the estimated state $\hat{\mathbf{x}}$ at corresponding altitudes. The sum of each row of AVK matrix is termed the measurement response (MR) which describes how sensitive the estimated state is to true atmospheric state. However, it is more convenient, here, to assess AVK and MR relative to the a priori profile. This, because x_a exhibits a strong vertical gradient and its covariance is scaled with x_a itself. As discussed in e.g. Baron et al. (2002); Hoffmann et al. (2011), the transformation from the ordinary AVK to the ‘fractional AVK’ matrix is given by,

$$250 \quad A_{ij}^{frac} = x_a(j) \cdot A_{ij} / x_a(i). \quad (12)$$

Accordingly, the ‘fractional MR’ is given by,

$$MR_i^{frac} = \sum_j A_{ij}^{frac}. \quad (13)$$

An example of the rows of the fractional AVK matrix and the corresponding MR of an inversion is shown in Fig. 3. As we can see these curves generally peak at their corresponding altitudes between 60~~40~~ km and 100 km where the line-of-sight
 255 tangent of the measurements lies. However, AVKs that represent $\hat{\mathbf{x}}$ above 100 km peak mostly around 100 km and their full width at half maximum (FWHM) become much larger. This indicates that the vertical resolutions of these altitudes are lower, which is a direct result of having no measurements at tangent altitudes above 100 km. The retrieval resolution is about 1-2 km below 90 km altitude. Figure 3 also shows the fractional MR. It has a value close to unity between 60~~40~~ and 100 km and quickly returning back to zero where no measurements are available. This indicates that the a priori profile has little influence
 260 on the estimated result between these altitudes. We use a fractional MR of 0.8 as the threshold to evaluate the quality of the estimated volume emission rate to present the remaining results and perform further analysis in this paper.

Besides MR, OEM also provides us with an analytical expression of the uncertainty in the estimated quantity. The covariance of retrieval noise is

$$S_m = \mathbf{G}S_e\mathbf{G}^T. \quad (14)$$

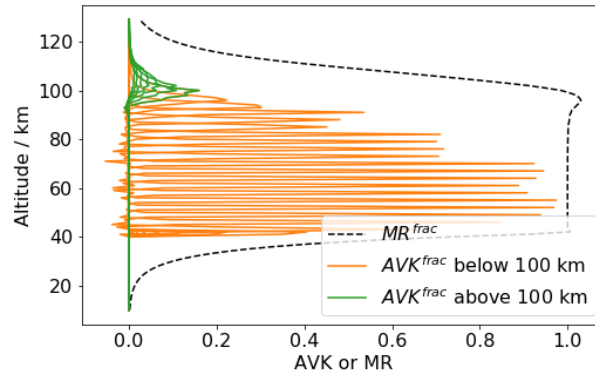


Figure 3. Every ~~two rows~~ third row of the fractional AVK (solid lines) and measurement response (black dashed line) from the retrieval of volume emission rate of the image 570 indicated in Fig. 4.

265 The diagonal elements of S_m will be treated as S_e in Sect. 2.3. ~~The uncertainty of the retrieved volume emission rate, together with the uncertainty of ozone, is presented later.~~

Figure 4 displays a typical example of the estimated volume emission rate and the error relative to the a priori, retrieved along one orbit. Only daytime measurements with a fractional MR greater than 0.8 are shown here. Two airglow layers can clearly be seen, separated by a minimum around 80 km and mixed with some finer structures between the layers. The relative error is
 270 generally under 25% above 70 km and under 10% below 70 km. Figure 4 also shows data gaps in a ‘zic-zac’ pattern, which are due to the nodding motion of the Odin satellite to facilitate the limb scanning process of the other instruments onboard (OS and SMR). Specifically, in this particular orbit, the satellite was in the so-called ‘mesospheric scan mode’ which results in data gaps up to 95 km. Hence, not all profiles can reach as low as 6040 km, as shown on the right panel of Fig. 4 (e.g. image 915). The first 3-4 nods in Fig. 4 correspond, however, to the ‘normal scan mode’ resulting in fewer data gaps.

275 2.3 Retrieval of ozone

Measurements of oxygen IRA band are often used as proxies to estimate daytime ozone concentration because the production of $O_2(a^1\Delta_g)$ is closely linked to the available ozone during the daytime. Measurements such as those from SME, SABER and SCIAMACHY have been used to estimate the ozone concentration using a chemical kinetic model and assuming photochemical equilibrium in a similar fashion (e.g., Thomas et al., 1984; Mlynckzak et al., 2007; Zarboo et al., 2018).

280 Estimation of ozone concentrations from airglow observation highly relies on the assumption of photochemical equilibrium as well as an accurate chemical kinetic model that relates the volume emission rate to the ozone number density. ~~Reaction~~
Using a photochemical equilibrium model will lead to under-estimate ozone concentration if the equilibrium state is not yet reached at a given time and location. Odin takes measurements in a 6h-18h polar orbit, thus a considerable portion of the daytime orbit is close to the sunrise, especially in the equatorial region. The closer to the sunrise the further the $O_2(a^1\Delta_g)$
 285 is from the equilibrium state, because of the dominant source of the emission being the solar photolysis. Thus, in this paper,

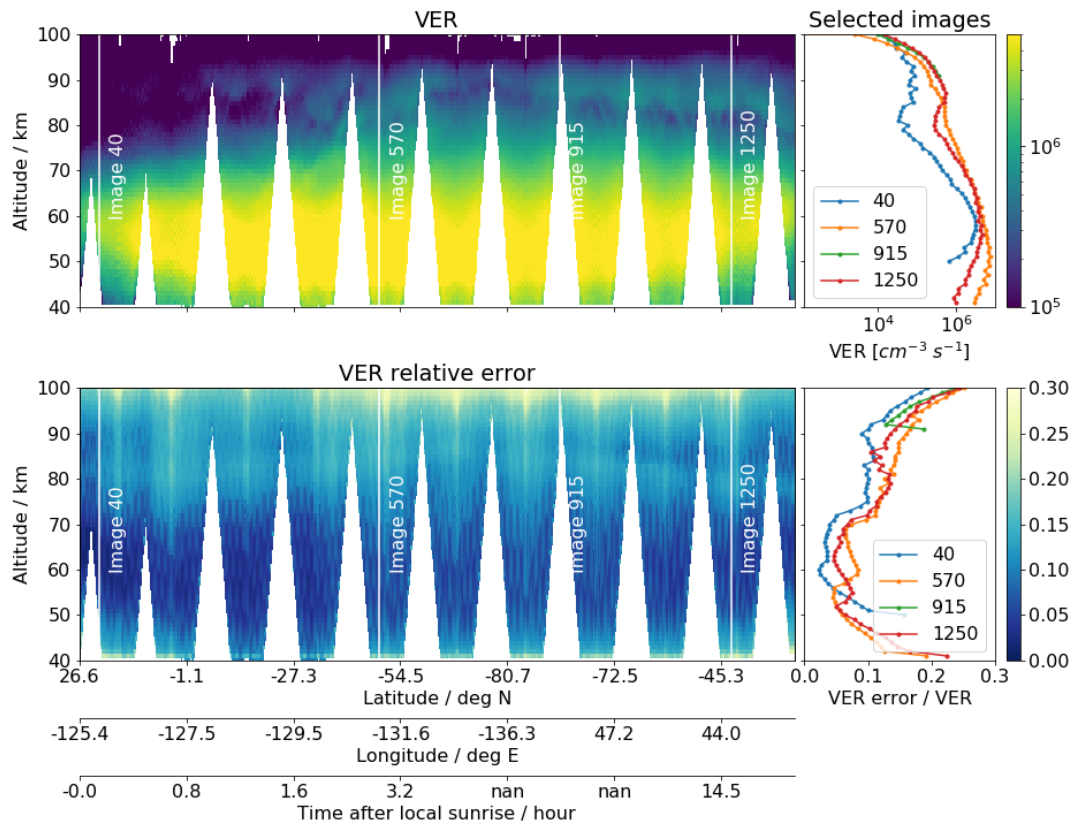


Figure 4. Example of the retrieved volume emission rate of $O_2(a^1\Delta_g)$ from IRI during daytime for one orbit collected on 2008-1-2, from 15:14:24 to 16:2:31 (orbit number 37400) and its error size relative to the individual a priori profile (upper and lower panels, respectively). The panels on the left are 2D-colour plots, as a function of geographical location and altitude. Time after local sunrise is also shown in the horizontal axis, and with 'nan' labels the panel sunrise is absent at the summer pole. The panels on the right are the cross section of the four selected images (along the four black solid white lines on the left panels). All results shown here have a measurement response greater than 0.8.

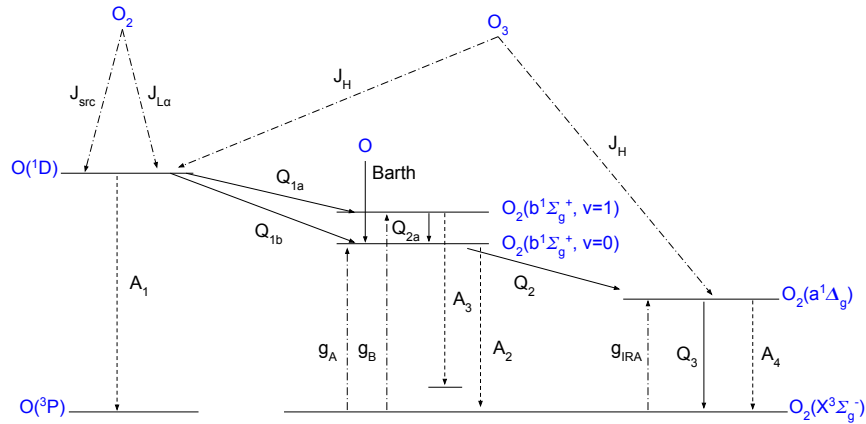


Figure 5. Scheme of kinetics of excited levels of atomic oxygen and molecular oxygen that are used in our model. Detailed reactions are described in Table A1

we apply a special treatment on the ozone retrieval where the photochemical steady state assumption can not be considered as valid. This will be described in Sect. 2.3.3.

In addition, reaction processes, Einstein coefficients, reaction rates, photolysis rates, reaction efficiency, solar irradiance, and such must be described as correctly as possible in the chemical model. In the early 1980s, R. J. Thomas et al. (1983) developed a simple photochemical model which only included ozone photolysis in the Hartley band and solar excitation of O_2 in the atmospheric band. This model was applied to SME $O_2(^1\Delta)$ measurements to derive ozone. After that, Mlynczak et al. (1993) showed that the photolysis of O_2 in the Schumann-Runge continuum and Lyman alpha spectral region make significant contributions to the $O_2(a^1\Delta_g)$ production through $O(^1D)$ production at higher altitudes. They concluded that the previous model led to an over-estimation of the ozone concentration from $O_2(a^1\Delta_g)$ observations. Accompanying the launch of SABER, in 2001, this model was further updated, the radiative lifetime of $O_2(a^1\Delta_g)$ was revised and other minor modifications were made, in order to derive ozone profiles from SABER $O_2(a^1\Delta_g)$ measurements (Mlynczak et al., 2007). Yankovsky and Manuilova (2006) have concluded that supplementing the vibrational states in the comprehensive photochemical model helps to get a better agreement between the ozone profiles retrieved from 1.27 μm and 762 nm emissions, based on a numerical experiment on a few METEORS rocket profiles (Mlynczak et al., 2001). Their model includes 3 vibrational levels of $O_2(b^1\Sigma_g^+, v=0, 1, 2)$, 6 of $O_2(a^1\Delta_g, v=0-5)$ and 35 of $O_2(^3\Sigma, v=0-34)$. Yankovsky et al. (2016) have used the same model to simulate how various oxygen airglows perform as proxies for atomic oxygen and ozone.

2.3.1 The kinetic model

In this paper, we use a kinetic model with the inclusion of two vibrational levels of $O_2(b^1\Sigma_g^+, v=0, 1)$, the Barth-type chemical mechanism (McDade et al., 1986), as well as the solar resonance absorption in the oxygen IRA band itself, which can be

305 described as a model whose the complexity is in between the one used by Mlynczak et al. (1993) and the one used by Yankovsky et al. (2016). Figure 5 illustrates the kinetic scheme of our model. Neglecting most of the vibrational sub-levels of each electronic state should not greatly affect the accuracy of the retrieved ozone. This can be considered as a reasonable assumption, because the population of the electronic-vibrational excited states is mostly dominated by the lowest vibrational state in each electronic level, and these sub-levels are eventually quenched to the lowest vibrational levels as shown by Yankovsky and
 310 Manuilova (2006). The processes that we have considered in our kinetic model are listed briefly below, while detailed reactions, as well as the corresponding rate coefficients and quantum yields or efficiencies, can be found in Table A1.

- J_H : photodissociation of ozone in the Hartley band ($\lambda < 310$ nm) produces the electronically excited state atomic oxygen $O(^1D)$ and molecular oxygen $O_2(a^1\Delta_g)$;
- $J_{SCR}, J_{L\alpha}$: photodissociation of ground state molecular oxygen in both the Schumann-Runge continuum ($130 \leq \lambda \leq$
 315 175 nm) and at Lyman α ($\lambda = 121.6$ nm) produces ground state $O(^3P)$ and excited atomic oxygen $O(^1D)$;
- g_A, g_B, g_{IRA} : resonance absorption of ground state molecular oxygen at A-band (762 nm), B-band (688 nm) and oxygen IRA band (1270 nm), respectively;
- Q_{1a} : transfer of energy by quenching $O(^1D)$ with $O_2(^3\Sigma)$ partly forms ground state atomic oxygen $O(^3P)$ and an excited level of molecular oxygen $O_2(b^1\Sigma_g^+, v=1)$;
- 320 - Q_{1b} : same as Q_{1a} but to form $O_2(b^1\Sigma_g^+, v=0)$;
- Barth: recombination between two oxygen atoms that through energy transfer processes produce $O_2(b^1\Sigma_g^+)$, known as the Barth-type mechanism;
- Q_{2a} : quenching of $O_2(b^1\Sigma_g^+, v=1)$ to the lower vibrational level $O_2(b^1\Sigma_g^+, v=0)$.
- Q_{2b} : quenching of $O_2(b^1\Sigma_g^+, v=0)$ to the lower electronically excited state of molecular oxygen $O_2(a^1\Delta_g)$;
- 325 - Q_3 : quenching of $O_2(a^1\Delta_g)$ to the ground state $O_2(^3\Sigma)$;
- A_1, A_2, A_3, A_4 : the inverse of photochemical lifetime of $O(^1D)$, $O_2(b^1\Sigma_g^+, v=0)$, $O_2(b^1\Sigma_g^+, v=1)$ and $O_2(a^1\Delta_g)$, respectively, when they eventually release their energy as a photon and transfer back to the ground electronic state.

Figure 6 shows the contributions from different production sources to $O_2(a^1\Delta_g)$ in the altitude range 60 to 150 km, both in percentage and absolute concentrations. The simulation is based on a single ozone profile taken from CMAM, a back-
 330 ground density and a temperature profile taken from the MSIS climatology (Pieone et al., 2002) at different solar zenith angles. Percentage-wise, photodissociation of molecular oxygen in both Schumann-Runge continuum and at Lyman α dominate above 100 km, which is consistent with Mlynczak et al. (1993). Below 100 km $O_2(a^1\Delta_g)$ is mainly produced by photodissociation of ozone in the Hartley band as well as by resonance absorption in the A-band. Resonance absorption in the oxygen B-band and oxygen IRA band contribute as much as 6% at around 80 km or even higher at around 115 km. Moreover, O_2 photodissociation

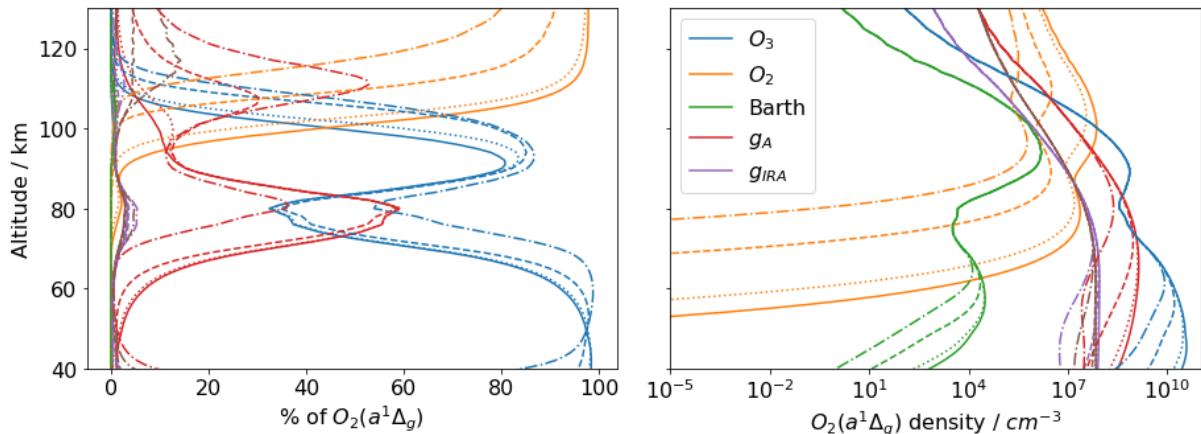


Figure 6. Left panel: relative contributions of 6 different sources to the production rate of $O_2(a^1\Delta_g)$ at 4 solar zenith angles, namely 30° (solid lines), 60° (dotted lines), 85° (dashed lines) and 89.9° (dot-dashed lines). Right panel: same as left, but in absolute concentration of $O_2(a^1\Delta_g)$.

335 in the altitude range of 60-150 km is highly sensitive to the solar zenith angle while the other photochemical sources are only sensitive below 90 km or below. The Barth-type mechanism contributes very little and mainly between 100-110 km. However, the Barth-type mechanism is the only source during the absence of sunlight since all the other sources involve photochemical reactions, which explains why the nightglow is much weaker than the dayglow (not shown in this paper).

Without simultaneous measurements of $O_2(b^1\Sigma_g^+)$, a reasonable assumption on the efficiency of $O(^1D)$ quenched by ground state O_2 to $O_2(b^1\Sigma_g^+)$ is needed. We assume that 20% are quenched to $O_2(^1\Sigma, v=0)$ and that the rest are quenched to $O_2(^1\Sigma, v=1)$, as indicated by Yankovsky et al. (2016). All $O_2(^1\Sigma, v=1)$ are assumed to be quenched by O_2 and N_2 to $O_2(^1\Sigma, v=0)$. Uncertainties in other reaction rate coefficients and their sensitivity to the retrieved ozone concentration are further discussed in Yankovsky et al. (2016).

345 By assuming photochemical equilibrium for $O(^1D)$, $O_2(b^1\Sigma_g^+)$ and $O_2(a^1\Delta_g)$, one may establish a system of equations to solve for the ozone concentrations from the measured oxygen IRA band volume emission rate. However, it is not straight forward to simply invert the system of equations as the model is non-linear. For example, calculating the solar photolysis rate in the Hartley band and calculating the atomic oxygen density for the Barth-type mechanism depend on how much ozone is present.

2.3.2 The inversion method

350 We choose to implement-use the Levenberg-Marquardt algorithm-method to retrieve the ozone number density iteratively (Rodgers, 2000). The ozone number density x at each iteration $n+1$ is derived using the formula

$$\mathbf{x}_{n+1} = \mathbf{x}_n + [(1 + \gamma)\mathbf{S}_a^{-1} + \mathbf{K}_n^T \mathbf{S}_e^{-1} \mathbf{K}_n]^{-1} \mathbf{K}_n^T \mathbf{S}_e^{-1} [\mathbf{y} - \mathbf{F}(\mathbf{x}_n)] - \mathbf{S}_a^{-1} [\mathbf{x}_n - \mathbf{x}_a], \quad (15)$$

where γ is the damping parameter and \mathbf{y} is the previously estimated volume emission rate profile (i.e. $\hat{\mathbf{x}}$ in Sect. 2.2) with a measurement response larger than 0.8.

355 In our implementation, all negative volume emission rates are treated as invalid and replaced by an interpolated value. $\mathbf{F}(\mathbf{x}_n)$ is the volume emission rate evaluated by the photochemical model and \mathbf{K}_n is the numerically calculated Jacobian at the n -th iteration based on $\mathbf{F}(\mathbf{x}_n)$. All negative ozone number densities are forced to be 10^{-8} cm^{-3} in $\mathbf{F}(\mathbf{x})$. \mathbf{S}_e is a diagonal matrix ~~taken from the retrieval~~ which refers to the result of previous retrieval step, being the retrieval noise of the volume emission rate (i.e. \mathbf{S}_m in Eq. 14). However, this measurement uncertainty matrix is further modified to address the issue of the validity
 360 of the photochemical equilibrium assumption at a given time and location. The details will be discussed in Sect. 2.3.3. All off-diagonal elements in \mathbf{S}_m are ~~set to zero~~ removed because the inversion of the full matrix often leads to numerical instability. We use the ozone profiles taken from the CMAM climatology as \mathbf{x}_a . \mathbf{S}_a follows the same formula as in the retrieval of volume emission rate (see Eq. 2.2), also with $\sigma_a = 0.75\mathbf{x}_a$. As the Levenberg-Marquardt method is an iterative procedure to solve non-linear problems, it requires an initial guess. We use \mathbf{x}_a for this. The background air density and temperature are taken from the
 365 MSIS climatology. The volume mixing ratio of O_2 , N_2 and CO_2 are assumed to be 21%, 78% and 405 ppm, respectively, at all altitudes. For the number density of O, we assume photochemical steady state with ozone.

When iteration has converged, γ is mostly sufficiently small ($\gamma \ll 1$) such that the retrieval can be approximated by using a Gauss-Newton method at the final iteration. Thus the relevant equations for the error analysis are essentially the same as Eq. 9 and Eq. 14 described in Sect. 2.2. Similarly, AVK and MR can be assessed using the Jacobian matrix at the final iteration.
 370 Finally, the ~~normalized~~ normalised cost of the retrieval is evaluated as

$$\chi_n^2 = [(\mathbf{x}_n - \mathbf{x}_a)^T \mathbf{S}_a^{-1} (\mathbf{x}_n - \mathbf{x}_a) + (\mathbf{y} - \mathbf{F}(\mathbf{x}_n))^T \mathbf{S}_e^{-1} (\mathbf{y} - \mathbf{F}(\mathbf{x}_n))]/m \quad (16)$$

where m is the number of elements in \mathbf{y} vector (here is the same as in \mathbf{x} vector, i.e. number of atmospheric layers).

~~An example~~

2.3.3 The photochemical equilibrium assumption

375 The inversion process described above highly relies on the assumption of photochemical steady state. As previously mentioned, if the $\text{O}_2(a^1\Delta_g)$ has not yet reached its equilibrium state at a given time and location, such an assumption will lead to an under-estimation of the derived ozone. The reason for this under-estimation is that since the O_2 contribution to the production of $\text{O}_2(a^1\Delta_g)$ is fixed, the low measured intensity of the $1.27 \mu\text{m}$ volume emission rate ends up being compensated as low or even negative values of ozone in the inversion process.

380 A considerable portion of the IRI measurements do occur close to the day-night terminator, and are therefore affected by this problem. In this section, we describe an extra step of the retrieval process intended to address this divergence from equilibrium when necessary.

Figure 7 attempts to illustrate a naive estimation of the ozone number density assuming photochemical equilibrium for all IRI measurements in one orbit. As the orbit proceeds (from left to right in Fig. 7), the effects of under-estimation of ozone can be seen where the measurements are made closer and closer to the local sunrise.
 385

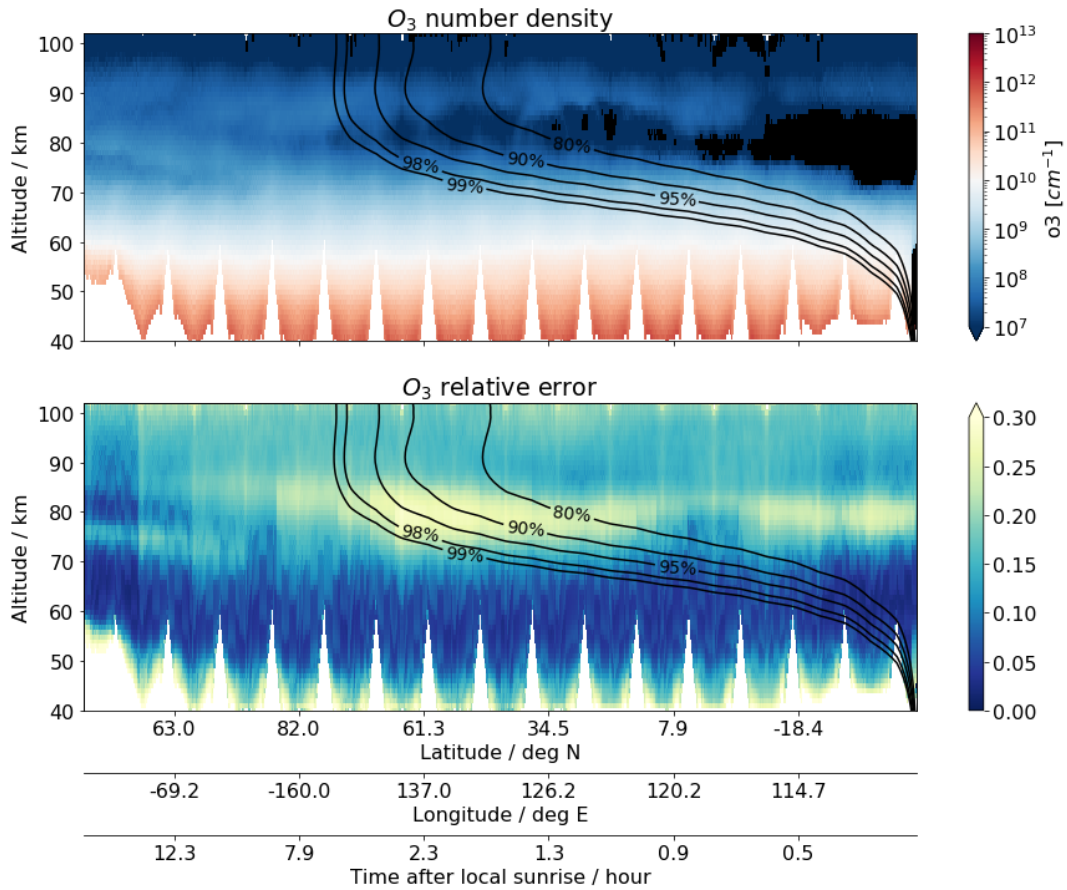


Figure 7. A naive estimation of ozone number density (upper) and its error size relative to the individual a priori profiles (lower) without the equilibrium index adjustment, for one orbit collected on 2008-03-30, from 22:21:09 to 23:09:13 (orbit number 38720), superimposed the contour lines of equilibrium index being 80%, 90%, 95%, 98% and 99% of the equilibrium level. Negative values are indicated as black colour. All results shown here have a measurement response greater than 0.8.

The change of the number density $[O_2(a^1\Delta_g)]$ can be described by a dynamical equation

$$\frac{d[O_2(a^1\Delta_g)]}{dt} = P - L[O_2(a^1\Delta_g)] \quad (17)$$

$$= P - \frac{[O_2(a^1\Delta_g)]}{\tau}, \quad (18)$$

where t is the time since the production has started (i.e. time after the local sunrise), P represents the production terms and L the loss rate of $O_2(a^1\Delta_g)$. The loss rate which is also the inverse of lifetime τ , consists of two components, the radiative relaxation and the collisional quenching (A_4 and Q_3 in Fig. 5). Assuming P and L are independent of time, one can provide a solution to the ordinary differential equation as

$$[O_2(a^1\Delta_g)] = [O_2(a^1\Delta_g)]_{equi}(1 - \exp(-t/\tau)), \quad (19)$$

where $[O_2(a^1\Delta_g)]_{equi} = P/L = \tau P$. Since A_4 is a fixed coefficient and Q_3 is mainly based on the background density for $O_2(a^1\Delta_g)$ kinetics, the lifetime τ can easily be calculated as a function of altitude. L is dominated by A_4 above 75 km while below is dominated by Q_3 . As the ratio t/τ to be 1.6, 2.3, 3, 4 and 4.6, $[O_2(a^1\Delta_g)]$ has reached 80%, 90%, 95%, 98% and 99% of the equilibrium level, which are indicated by the contour lines superimposed on Fig. 7. Thus, we can use $(1 - \exp(-t/\tau))$ as an equilibrium index to indicate how far the given time and location is from the equilibrium state.

To address the validity of the equilibrium assumption in the ozone retrieval, the uncertainty of the measurement vector S_e is further modified as

$$S_e^{modified} = S_e / (1 - \exp(-t/\tau))^8. \quad (20)$$

As a result of such a modification, the inversion will avoid updating the a priori profile giving a low measurement response in the region where the equilibrium assumption is far from valid, while S_e is barely modified where the equilibrium index is close to 100%. As shown in Fig. 8, the upper right region of the plots, where the equilibrium index is significantly lower than 100%, is blanked out due to the low measurement response, while the lower left part of the plots show no difference to the ones shown in Fig. 7. In addition, such an adjustment on S_e amplifies the represented error size where the equilibrium index is relatively lower, indicating that this part of the data set should be handled with care.

Two example images of the fractional AVK and MR is are shown in Fig. 9 indicating that the, which correspond to the images 40 and 1250 in orbit number 37400 (see Fig. 4). The first example image clearly shows that the measurement response is effectively dampened by $S_e^{modified}$ with a low equilibrium index above 65 km, while the second example image keeps a high measurement response at almost all altitudes. The full width at half maximum of the AVKs indicates that the vertical resolution of the ozone profiles is about 1-2 km where the data points are considered to be valid. Note that the AVKs above 90 km may not necessarily represent the 'true' values as the retrieval resolution of the oxygen-IRA-band volume emission rate is not properly taken into account in the ozone retrieval. Thereafter we present our results for all IRI ozone data points that have a fractional MR greater than 0.8 and χ^2 smaller than 10. The statistical representation of the uncertainties (i. e. retrieval

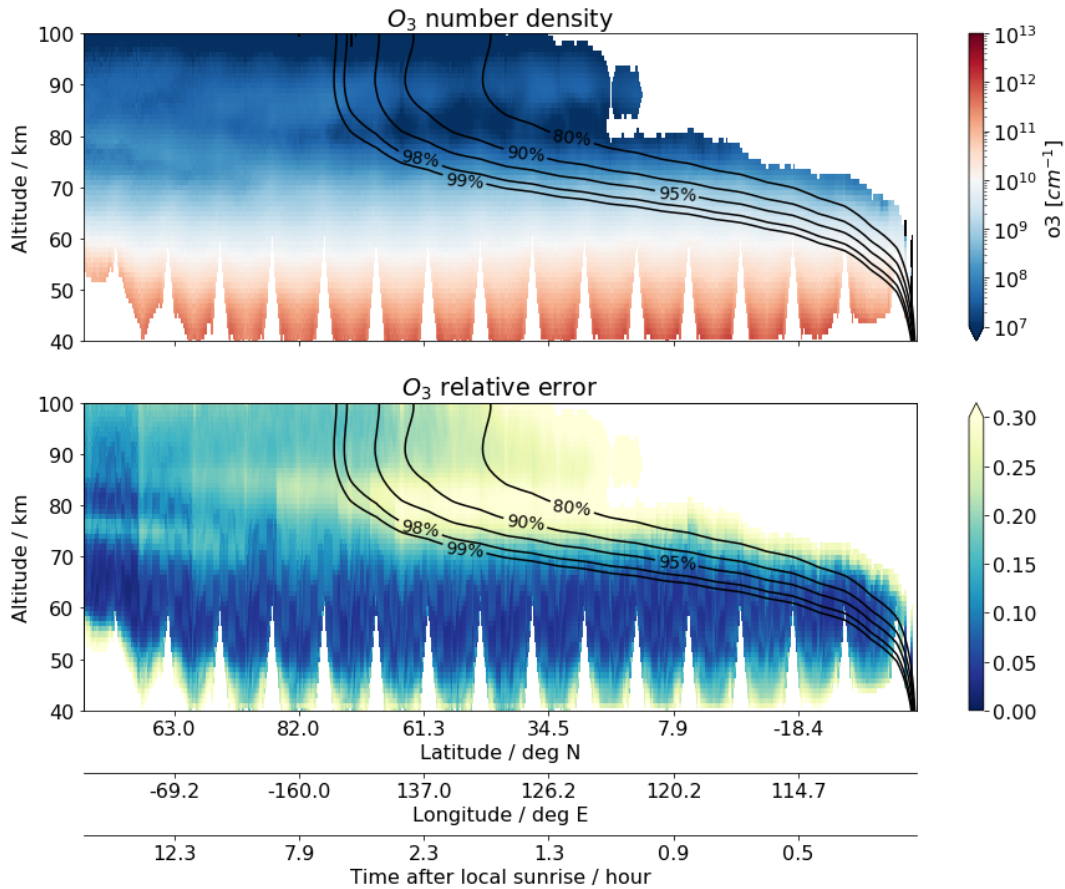


Figure 8. Same as Fig. 7, but showing the final estimation with the adjustment of the equilibrium index.

noise) of both the volume emission rate product and the ozone number density product 10 and equilibrium index corresponding to more than 95% of the equilibrium value. Also, the lowest 10 km grids in the retrieval are filtered out to avoid biases due to the possible edge effect. After all these criteria are used for filtering, the IRI ozone data availability at 80 km over one year (every 20th orbit) is presented in Fig. ??, sealed with their a priori profiles. The mean uncertainties on both are around 5-30% with larger values at higher altitudes where concentrations of and ozone are low. 10. A significantly high number of profiles is located in the summer polar region because of the 6-18h Odin orbit. No data is available at the tropics, at the altitude of 80 km, due to the fact that the measurements were made too close to sunrise.

Every two rows of the fractional AVK (solid lines) and MR (black dashed line) from the ozone retrieval of a sample image (the same image as in Fig. 3).

Overall, the resulting IRI mesospheric ozone product has a precision of around 5-20% based on the retrieval noise estimate (see bottom panel of Fig. 8), with relatively larger values above 80 km and below 50 km. However, the systematic error in the estimated ozone product is as large as 50% of positive bias which can be found in the comparisons with other ozone data

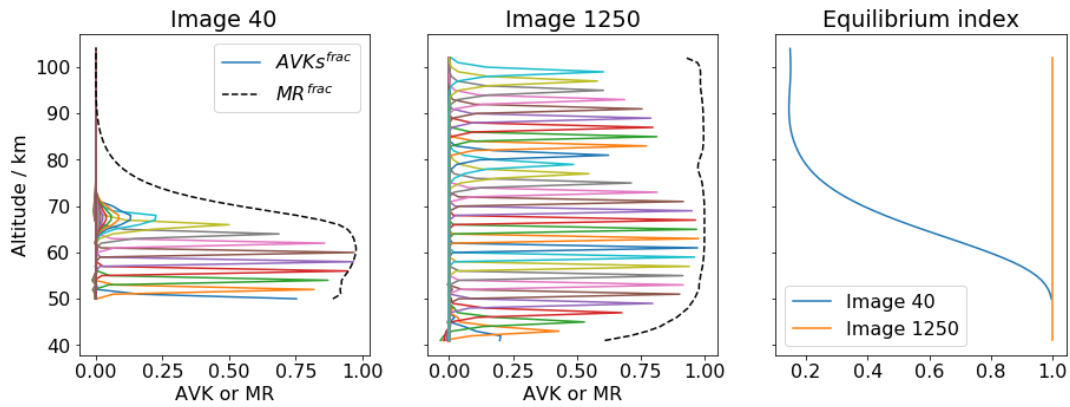
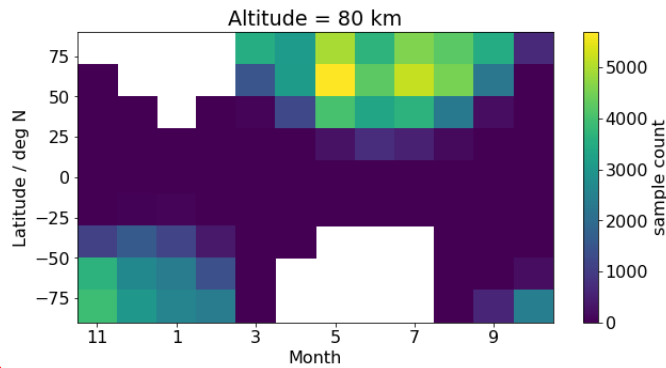


Figure 9. Every second row of the fractional AVK (solid lines) and MR (black dashed line) of the ozone retrieval for two example images (the first two panels) taken from the orbit number 37400 (see Fig. 4 for reference). The corresponding equilibrium indices of these two images are shown in the third panel.

The retrieval noise of the volume emission rate (in blue) and the ozone number density (in orange), scaled with their corresponding a priori profiles. Solid lines are the average-profile between Nov 2007 and Oct 2008 and the shaded areas indicate the standard deviation around the



averaged-uncertainties-

Figure 10. IRI ozone data availability at 80 km for a one-year sample data set (every 20th orbit), after validity criteria have been applied (see text). The number is expected to increase by 20 times when all the orbits of one year are processed.

Table 1. A summary of the possible sources to the systematic error in the IRI ozone and their relative sizes.

<u>Error sources</u>	<u>estimated sizes</u>
<u>Kinetic parameters in the photochemical model^a</u>	<u><20% below 90 km, >100% above 90 km</u>
<u>Absolute calibration^b</u>	<u><20%</u>
<u>Absorption correction factor</u>	<u><1%</u>
<u>Temperature dependent filter overlapping</u>	<u><1%</u>

a: see Yankovsky et al. (2016) as well as Mlyneczek and Olander (1995) for a comprehensive analysis on the sensitivity of each of the parameter

b: due to lack of in-flight calibration

sets (see Sect. 3.4). The detail investigation may be carried out in a future study when the 20-year-dataset has been processed. Moreover, the precise quantification of these error sources requires detail modelling studies and thus the focuses of this paper remain on the retrieval technique on deriving daytime ozone from the 1.27 μm emission. Here, we summarise the possible source to the systematic error and estimate their relative size to our best knowledge for the potential future data users (see Table 1).

3 Ozone comparisons

To illustrate the performance of the technique described in Sect. 2.1–Sect. 2.32, daytime ozone profiles have been derived for a test sample of 5 % (every 20th ~~orbits~~orbit) of all the limb measurements collected by IRI from November 2007 to October 2008. In order to show the fidelity-consistency of the results, these IRI ozone profiles are compared with independent ~~datasets~~data sets derived from OS, SMR, ~~MIPAS and ACE-FTS~~and MIPAS. We would like to emphasise that a comprehensive validation study is not the primary intention of this study, ~~which~~. This will be a valuable future study, after the ~~20-years data~~whole 20-year IRI data set has been processed. We choose to use mainly number density for the comparisons, as it is the natural unit of the IRI and OS ozone profiles. As pointed out by Smith et al. (2013), the differences in background densities to derive ozone VMR introduce additional uncertainty between instruments. As such, we would like to avoid using external data as much as possible. Moreover, the measurements of ozone by SMR at higher altitudes are mostly based on Doppler broadened lines, thus the natural unit is closer to number density rather than VMR. Therefore, the visualisation of the profile comparisons in this section is shown in ozone number density, with only one exception in the last panel of Fig. 11.

The ~~datasets-considered~~data sets under consideration are briefly described in Sect. 3.1. In Sect. 3.2, we compare coincident observations made by OS, IRI and SMR, all from one example orbit. Since they are on board the same spacecraft, numerous co-incident profiles can be found. Yet, the measurement principles of these three instruments are intrinsically different. ~~The comparison of the zonally averaged daytime ozone profiles from the five aforementioned instruments is discussed in Sect. 3.4. Lastly, in Sect.~~In Sect. 3.3, we will focus on the annual cycle of daytime ozone vertical structures in the MLT region. Lastly, ~~the comparison of the zonally averaged daytime ozone profiles from the four aforementioned instruments is discussed in Sect.~~

Table 2. Main characteristics of the ozone ~~datasets~~data sets under consideration

Instrument (satellite)	Version	Retrieval uncertainty	Vertical resolution	Vertical coverage	meas
IRI (Odin)	V1-0	5-20 %	1-2 km	60-100 <u>40-100</u> km	
OS (Odin)	V5-10	<5 %	2-4 km	10-60 km	
SMR (Odin)	V3.0.0	~ <u>1</u> ppmv	2.5-3.5 <u>3.5</u> km	18-65^c or 20-80^d <u>12-95</u> km	
MIPAS (Envisat)	V5R	5-10 %	4-8 km	5-100 km	
ACE-FTS (SCISAT-1) V4 < 3 % 3-4 5-95 VMR height					

a: Number density

b: Volume mixing ratio

3.4. Our goal is to illustrate the consistency of IRI ozone profiles with the other ozone products and, to a lesser extent, to interpret the differences between them.

3.1 Other ozone ~~datasets~~data sets

Although this is not a complete validation study, independent ozone ~~datasets~~data sets are used to compare with the new
455 ozone product. The main characteristics of these ~~datasets~~data sets are given in Table 2. We have selected measurements made between November 2007 and October 2008 by each of the instruments under consideration. A brief description of the measurement principles and data screening methods is provided in this section. More detailed information can be found in the cited publications.

3.1.1 OS

460 In previous publications, the term OSIRIS ozone product usually refers to the product obtained from the optical grating spectrograph (e.g., McLinden et al., 2007; Bourassa et al., 2018). In Smith et al. (2013), OSIRIS ozone refers to the product derived from the A-band airglow emission by Sheese (2009). In this paper, we will use OS ozone to refer to the product derived from the measured limb scattered sunlight in the Chappuis and Hartley-Huggins bands. These ozone profiles are retrieved from limb radiance pairs and triplets using the multiplicative algebraic reconstruction technique (MART) (Degenstein et al., 2009).
465 This ~~dataset~~data set is one of the OSIRIS operational products within the ESA Climate Change Initiative (CCI) programme ². Invalid values have already been screened out by the instrument team (Sofieva et al., 2013).

3.1.2 SMR

The sub-millimetre radiometer on-board the Odin satellite measures spectra at different altitudes during the limb scans. In particular, it measures the ozone thermal emission line at 545 GHz (this is the so-called frequency mode 2 in the SMR nomen-
470 clature). As described in Eriksson (2017), vertical profiles of ozone are retrieved based on the optimal estimation method

²ESA CCI programme: <http://cci.esa.int/ozone>

(OEM) by inverting the radiative transfer equation for a non-scattering atmosphere. This SMR ozone ~~dataset~~ [data set](#) has recently been reprocessed. In this study we use the new ozone main product of SMR, whose quality was assessed in Murtagh et al. (2018). This product is in much better agreement with other instruments, compared to the previous version. All data points that have a measurement response lower than 0.8 are considered as invalid values. Ozone volume mixing ratio (VMR) is provided and the ozone number density is determined by multiplying it with the background number density provided in the ~~dataset~~ [data set](#). This background number density comes essentially from the combination of ECMWF analyses and the MSIS model. All nighttime measurements (i.e. with the labelled solar zenith angle larger than 90°) are screened out [for analysis](#) as we only look at the daytime ozone distribution in this paper—, [except for in Fig. 11 for demonstration purpose](#).

3.1.3 MIPAS

480 The Michelson Interferometer for Passive Atmospheric Sounding measures the thermal emission line of ozone at $9.6\ \mu\text{m}$. We chose to use the middle atmospheric mode in our analysis. This ~~dataset~~ [data set](#) has been processed by KIT-IMK and documented in Van der A et al. (2017); López-Puertas et al. (2018). As for SMR, all nighttime measurements are excluded from further analysis. Following the MIPAS level 2 screening recommendations, all data points that are flagged by ‘visibility = 0’ or have an averaging kernel diagonal element of less than 0.03 are not considered. Ozone concentration is given in VMR. 485 We use the temperature and pressure measured by MIPAS to calculate the ozone number density.

3.1.4 ACE-FTS

~~The Fourier Transform Spectrometer on the Atmospheric Chemistry Experiment measures ozone along with temperature and pressure profiles by using the solar occultation measurement technique (Bernath et al., 2005). In contrast to measuring scattered sunlight such as done by OS, ACE-FTS aims at the sun directly through the limb and can therefore only measure a maximum of two profiles per orbit, greatly limiting the sampling frequency compared to the other instruments. The retrieval method is described by Boone et al. (2005). Ozone concentration is given in VMR. We use the measured temperature and pressure to calculate ozone number density. Following the version 4 data screening recommendations, all data points that are flagged ‘-999’ and ‘-888’ are filtered out. In addition, data points associated with a statistical error for ozone VMR larger than 2 are not considered in our analysis.~~

495 3.2 ~~Coincident comparison~~ [Comparison of coincident profiles](#)

As mentioned in the earlier sections, the Odin satellite collects ozone profiles from three independent instruments. SMR measures thermal emission of an excited state of ozone in the microwave region at 545 GHz, OS measures scattered solar light in the Hartley-Huggins and Chapuis bands and IRI measures the oxygen airglow emission at oxygen IRA band. Due to the underlying measurement principles of these ~~datasets~~ [data sets](#), the altitude ranges and parts of the orbit during which data is available vary. This is depicted in Fig. 11. For this particular example orbit, SMR ~~ozone measures from 10~~ [measures ozone from 15](#) to a maximum ~~80~~ [75](#) km altitude both daytime and nighttime throughout ~~the~~ [this particular](#) orbit, while OS measures

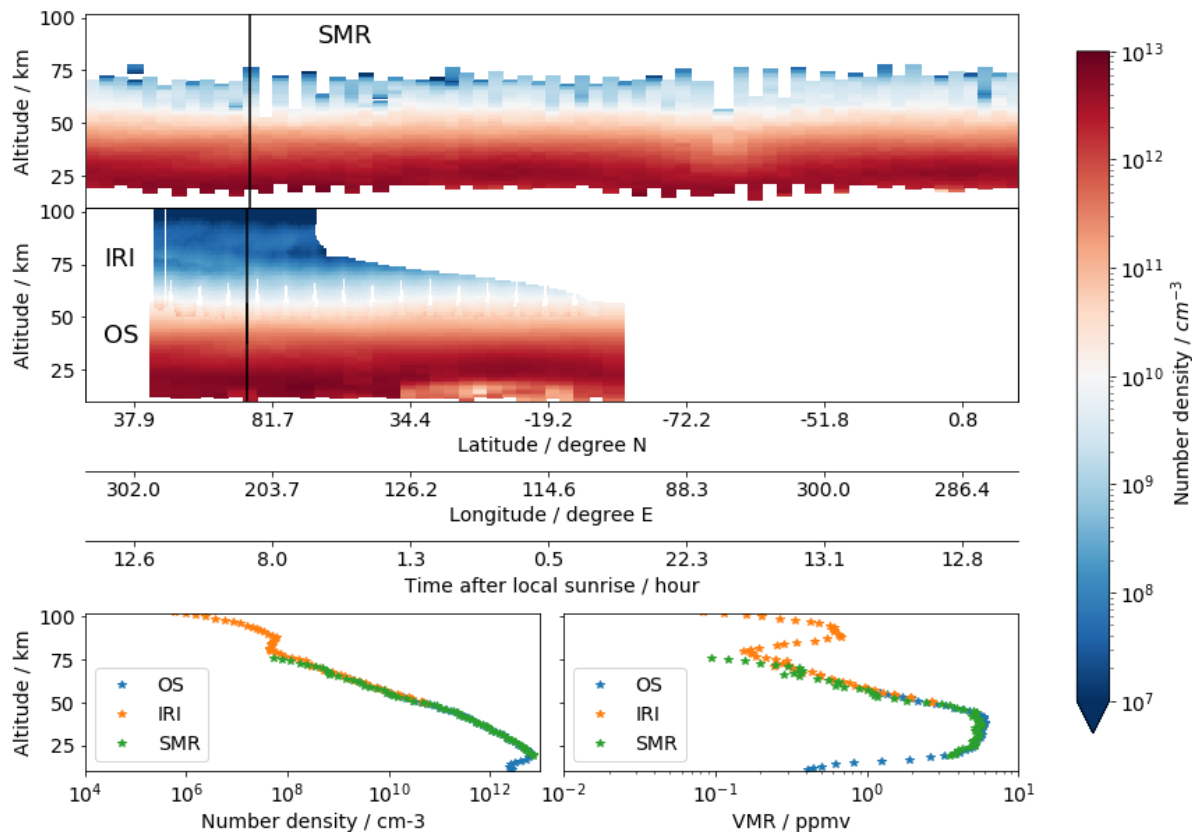


Figure 11. Upper panel: 2D-colour plot of SMR ozone number density profiles for one orbit as function of altitude and geographical location, collected on 2008-3-30 from 22:14:56 to 23:51:03 (Odin orbit number 38720). Middle panel: 2D-colour plot of IRI (above 40 km) and OS (below 60 km) daytime ozone profiles corresponding to the same orbit as SMR. Bottom left: ozone number density profiles from the scan/image of OS, IRI and SMR indicated by the black vertical line in the panels above. Bottom right: same as the bottom left panel but showing the volume mixing ratio in ppmv.

ozone only up to 55 km and during only half of the orbit, where scattered sunlight is available. IRI ozone covers the altitude range from 60–50 to 100 km as limited by the VER retrieval grid and measurement response (see sections 2.2 and 2.3). IRI ozone is also limited to the day part of the orbit since the oxygen airglow primarily relies on photochemical reactions, as discussed in Sect. 2.3.

It is worth mentioning that Fig. 11 also illustrates the particularly high sampling rate of IRI, over 70 times higher than SMR and OS due thanks to the imaging sensor. The bottom left panel of Fig. 11 shows a single ozone density profile collected at the same time and location by all three instruments. The volume mixing ratio of IRI ozone is derived based on the background density included in the SMR product (see Sect. 3.1.2) and is shown in the bottom right panel of Fig. 11. Both the primary and secondary ozone layers appear clearly in the plots. These two plots suggest that these coincident ozone profiles would merge

smoothly with each other, even though they do not cover the same altitude ranges. This result shows how consistent the ozone observations from these three instruments aboard Odin are with each other, despite the fact that they use intrinsically different measurement techniques, even though the agreement between IRI and SMR ozone relatively worsen above 65 km. However, if one meticulously studies the 2D-colour plot of the IRI ozone in the mid-panel of Fig. 11, some vertical stripes may appear following the scanning pattern. ~~This effect is probably~~ We believe that this effect is a result of the stray light correction process in the level 1 data (See Sect. 2.12.1.3).

3.3 Monthly mean time series comparison

In this section, we show the monthly mean daytime ozone distribution in the MLT region as presented in an altitude-time series for different latitude bands. We will look at the data sets in ozone number density from three instruments side-by-side, namely IRI, SMR and MIPAS.

3.4 **Zonal-average comparison**

~~Figure 13 depicts one example month of ozone distribution in number density for the five different instruments, averaged in 10~~ Figure 12 shows the monthly mean ozone number density in the MLT region for six latitude bands: 70-90°, 50-70° latitude bins (upper panels) and the corresponding profile count in each latitude bin (lower panels). In this case, December 2007 is shown. Although the vertical coverage of individual profile may differ, IRI shows a great advantage with a significantly higher sampling rate than the other instruments. Note that only every 20th orbits of IRI measurements have been processed in this study. Once all orbits are processed, the number of profiles will be roughly 20 times higher. The latitudinal distribution of the stratospheric main ozone layer (below 60 and 30-50° in both hemisphere. The low latitude region is not shown due to the lack of IRI data above 80 km) is in overall good agreement between OS, SMR, ACE-FTS and MIPAS, where ozone peaks at as expected from Fig. 10. It is recognisable that IRI ozone data set can reproduce the general seasonal pattern in the MLT, similarly to the other data sets. For all instruments at high-latitude, the top of the primary ozone layer extends to a higher altitude in the equatorial region and lower in polar regions, nearly symmetric with respect summer months, while relatively stable when moving closer to the equator.

~~In the MLT region (above 60), the latitudinal distribution and the strength of the Brewer-Dobson circulation of stratospheric ozone as discussed in Kyrölä et al. (2010). The secondary ozone maximum seem to be less consistent among IRI, SMR, ACE-FTS and MIPAS. IRI observes a deep ozone trough (i. e. the minimum separating the two ozone layers) concentrated in the mid-high latitude towards the winter pole centred at 75 in the mesosphere at high-latitudes is located at roughly the same altitude of ca. 90 km . The ozone trough is so deep that the estimated values can include negative values due to the weak volume emission rate and measurement uncertainty and therefore blanked out in Fig. 13. SMR observations agree well with IRI, with the ozone trough in the northern hemisphere so deep that the measured signal is too weak to give valid data. ACE-FTS, however, observes a deeper ozone trough in the summer hemisphere than IRI, while comparison in the winter hemisphere is not possible due to lacking overlapping data. MIPAS observes a deeper trough in the winter hemisphere as among these ozone data sets. At mid latitudes, the secondary ozone layer is slightly lower in altitude~~

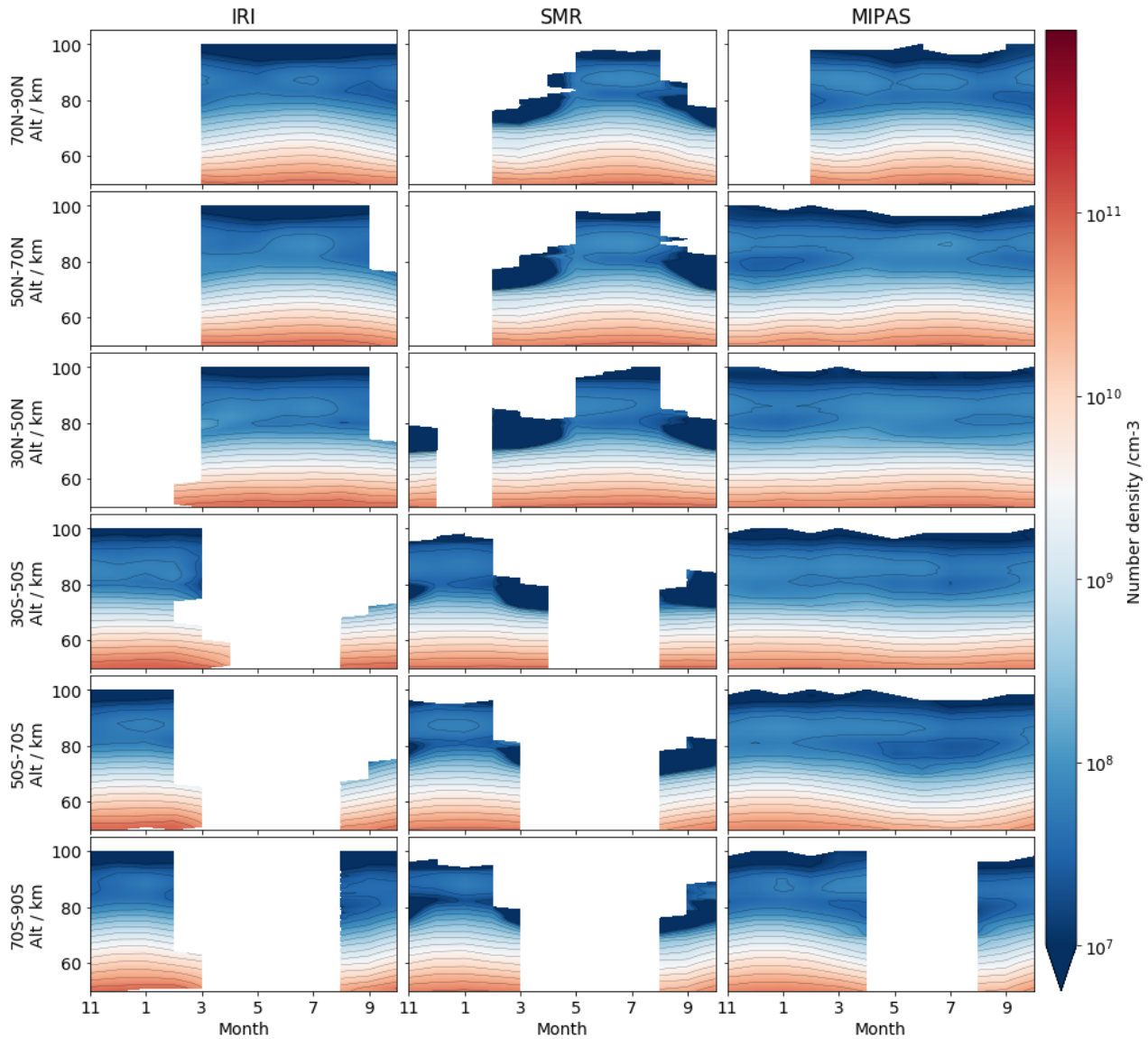


Figure 12. Upper-panel: 2D-colour-plot of SMR Monthly mean ozone number density profiles for one-orbit as function of altitude and geographical location, collected on 2008-3-30 from 22:14:56 November 2007 to 23:51:03 October 2008, in six selected latitude bands (Odin orbit number 38720 in rows). Middle-panel: 2D-colour-plot of IRI (above 60) and OS (below 60) daytime ozone profiles in the same orbit as SMR. Black colour indicates that the estimated ozone value is negative. Bottom-left: ozone number density profiles Columns from the scan/image of OS, left to right represent IRI and SMR indicated by the black vertical line in the panels above and MIPAS, respectively. Bottom right: same as the bottom-left panel but volume-mixing ratio in -.

(ca. 85 km). This is consistently observed by all three instruments. A deep ozone trough between the main and the secondary layers is observed by MIPAS in the winter months in the high-latitude bands, while IRI and SMR lack of data in those region because Odin was orbiting in the night part of the orbit. Overall, IRI agrees well with MIPAS, and, to a lesser extent, with SMR due to the fact that very low (sometimes negative) values exist in the regions between the secondary and primary ozone layer. All instruments display a weaker secondary maximum in the lower latitude than in IRI and SMR data, but a relatively even distribution in the MLT region. Nevertheless, all of these instruments display an ozone trough lower in altitude towards the winter pole. This latitudinal asymmetry may be the result of the pole-to-pole meridional circulation. The asymmetric pattern of the ozone trough follows an annual cycle which can be studied in Fig. 12 more easily. higher latitude regions, which is also shown by Smith et al. (2013) and may be explained by the tidal effects as mentioned in López-Puertas et al. (2018). We are going to look at the differences between these three instruments in more details in the next section.

One must be cautious when looking at such a zonal average comparison. Ozone production and loss rates depend on solar zenith angle (SZA), and their dependency varies with altitude. Especially in the MLT region, the ozone concentration changes drastically at sunrise and sunset (Allen et al., 1984; Huang et al., 2008), (see also the diurnal variation of ozone estimated from the NCAR ROSE model in Kyrölä et al. (2010) their Fig. 8). The sampling patterns of the three satellite platforms considered in this paper are shown in Fig. ?? OS,

3.4 Latitudinal distribution

Here, we focus on a selected month when IRI has a reasonably good latitudinal coverage to compare our newly derived data set with OS, SMR and MIPAS ozone in a more detailed manner, by looking at both a side-by-side comparison of the general global distribution and relative differences in different latitude bands.

Figure 13 depicts the daytime ozone distribution in number density, as observed in July 2008 by the four instruments under consideration, averaged in 10° latitude bins (upper panels). The 2D-histograms of the sample count in each latitude-altitude bin is also shown in the lower panels. The overall side-by-side comparison demonstrates that the IRI data set is capable of representing the general latitudinal distribution of ozone in the MLT, and complements well the already existing OS data set with the potential to merge with it. The secondary ozone layer around 90 km that peaks in the summer high latitude region can be observed in IRI, SMR and MIPAS, as expected from the seasonal trend shown in Fig. 12. SMR shows a region of very low or even negative values due to low measured signal around 80 km. Apart from the peak at 90 km at high latitudes in the summer hemisphere, another weaker peak can be observed in the winter hemisphere in the MIPAS data set. Unfortunately, this can not be observed by IRI and SMR orbit the Earth close to the day-night terminator with SZA in the range 60-90 with the lower angles towards the summer pole. ACE samples exactly at sunrise and sunset due to the lack of daytime measurement in that region because of the Odin orbit.

Although the vertical coverage of the individual profiles may differ, IRI shows a great advantage with a significantly higher sampling rate than the other instruments. Note that only every 20th orbit of IRI measurements has been processed in this study. Once all orbits are processed, the number of profiles are expected to be roughly 20 times higher. The 2D-histograms show that the sample size is significantly larger at high Northern latitudes than in the equatorial region for all instruments on board Odin,

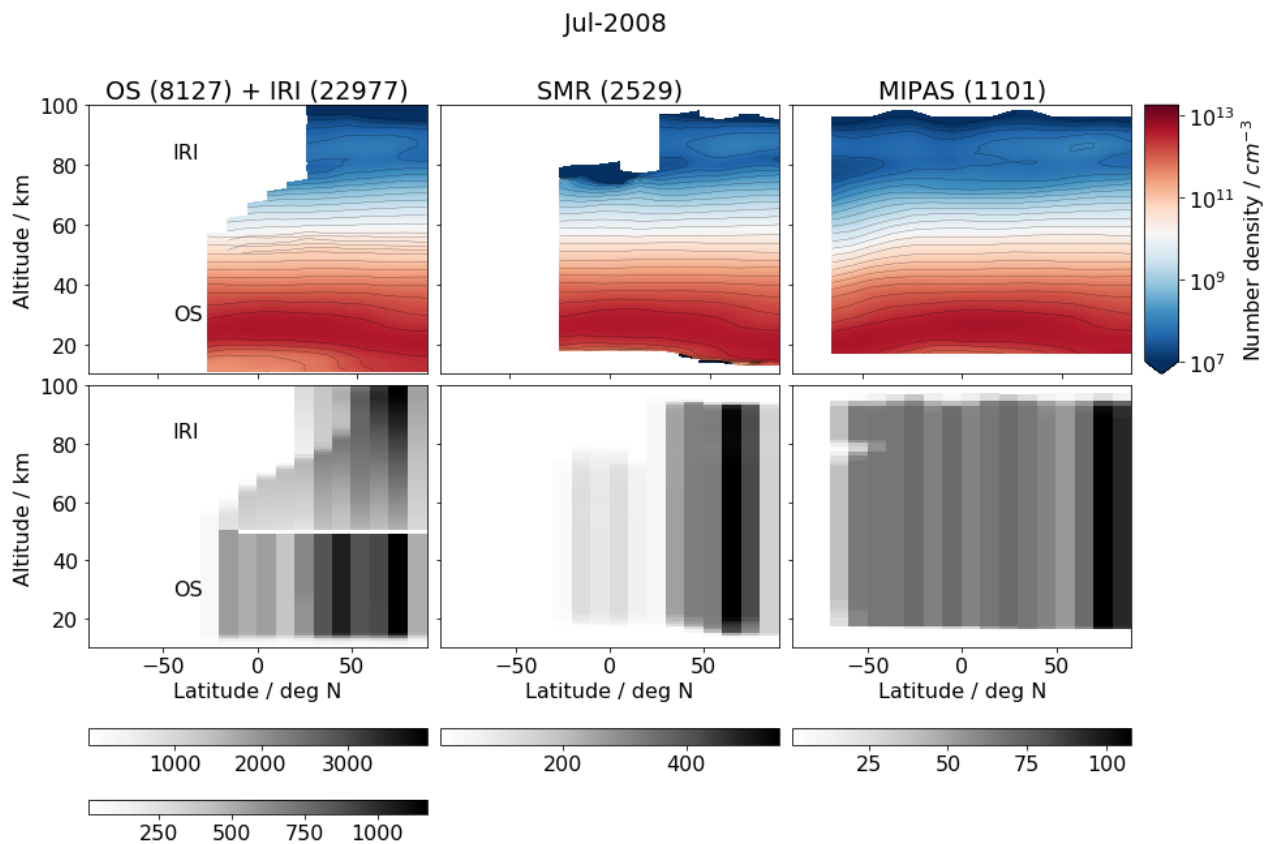


Figure 13. Zonally averaged daytime ozone number density observed in July 2008, with 10° latitude bins. The first column contains data from two instruments, with OS below 60 km and IRI above 50 km. The second and third columns correspond to SMR and MIPAS, respectively. The numbers in brackets indicated in the titles are the total number of profiles that are available within the month under consideration. Bottom panels correspond to 2D-histograms showing the number of samples that are accounted for the zonal average bins. Note that the colour scales of 2D-histograms are different in the bottom panels. The upper colour bar of the 2D-histogram in the left corresponds to IRI and the bottom one corresponds to OS.

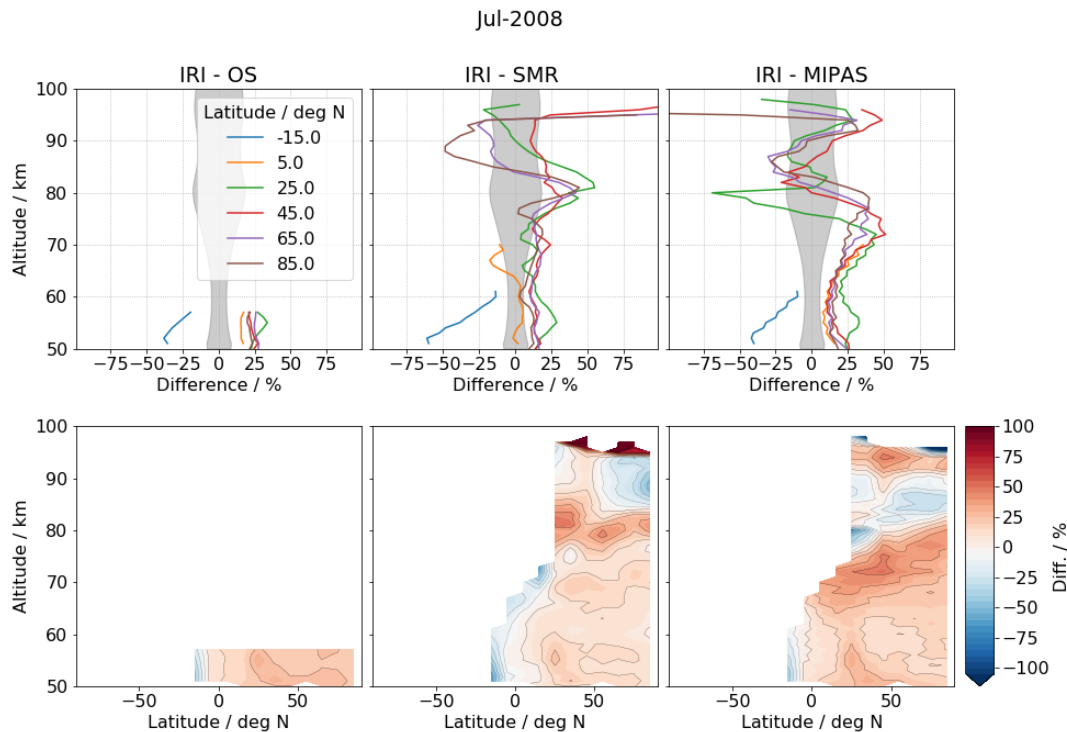


Figure 14. Zonal-average Relative difference of the zonally averaged ozone number density observed in December 2007/July 2008, with within 10° latitude bins. The first 2D-colour plot contains data from two instruments, with OS below 59, SMR and IRI above 60. The second MIPAS relative to fourth 2D-colour plots correspond to SMR/IRI are presented in first, ACE-FTS second and MIPAS third column, respectively. The numbers in brackets, indicated in the titles, Upper and lower panels are the total number 1D and 2D representation of samples (profiles) that are available within the month under consideration this difference, respectively. Black colour indicates negative The mean IRI ozone value. Bottom panels correspond to histograms showing the number of profiles that are accounted for the zonal averages. Note that the scales of the vertical axes are different percentage error is also shown in grey colour in the bottom upper panels.

while MIPAS samples at SZA between 22 and 90 has a more evenly spread observation distribution, with still more data in the summer pole. Also, due to the equilibrium index filtering (see Sect. 2.3.3), IRI loses most of the data above 70 km with the lower angles around the equatorial region and higher angles in the polar regions. It is also worth mentioning that the number of observations can differ by several orders of magnitude in each latitude and altitude bin, as seen in the lower panels of Fig. 13. km in the tropics, since they were mostly measured very close to the local sunrise. As mentioned in Sofieva et al. (2014), insufficient or inhomogeneous sampling can result in inaccurate average estimates. However, a complete investigation of the sampling uncertainty is beyond the scope of this paper.

The sampling patterns of the instruments on three spacecrafts with respect to the local solar zenith angle (SZA) during December 2007, as function of latitude.

For a more detailed comparison, a single latitude bin is selected and the ozone number density measured by the five instruments are depicted in Fig.?? (left panel). The Figure 14 shows the relative differences between IRI and the other data sets, i.e. $(\text{IRI} - \text{Instrument})/\text{IRI}$, for the ozone zonal mean profiles agree well with each other below 60 measured in July 2008 (other months show similar results). A general positive bias in IRI, with some exceptions at higher altitudes, can be seen in this figure. In the region below 70 km. Regarding the mesospheric data, there is good agreement on the average magnitude of the secondary maximum located at 90 km. However, the depth of the ozone trough differs between these ozone datasets. Figure ?? also depict the relative differences (right panel) to the OS (below 60, IRI has a positive bias of up to 25% compared to all three instruments. Above 70 km) or IRI (above 60) zonal mean profile. SMR agrees relatively well with IRI with a maximum of 20% difference around the ozone trough region. MIPAS exhibits a difference of maximum, a positive bias of up to 50% relative to IRI since the height of the secondary layer is slightly off-set. The disagreement of MIPAS would probably be better if we would take into account the vertical resolution correctly of all the instruments. ACE-FTS appears to have as large as 70% difference at the minimum (is observed around 75 km compared to MIPAS, and similarly to SMR but observed around 80 km) and at the top of the secondary ozone layer (above 95, However, between 80 to 90 km). These differences are expected since the ozone density at the trough and above the peak is so low that relative uncertainties become very large.

A comparison of zonal mean profiles between the five instruments for a selected latitude bin (30—40°S) in December 2007. The left panel shows the absolute comparison in number density and the right panel shows the relative difference to the OS and IRI zonal mean profiles.

3.5 Monthly mean time series comparison

In this section, we focus on ozone comparison in the MLT region. As can be seen in Fig. 13, OS rarely collects ozone profiles in the region where IRI measures. We will therefore only look at the ozone number density from four instruments: IRI, SMR, ACE-FTS and MIPAS.

Figure 12 shows the monthly mean ozone number density in the MLT region for three latitude bands: 30-50, negative differences of about 25% are observed compared to MIPAS, with an exception in the latitude band 20-30 deg N where the differences are bigger, up to -70%. In comparison with SMR, between 85 to 95 km, the differences vary from -25% to +10% (except for latitudes above 80 deg N, with differences up to -50%) depending on the latitude bands, with larger negative bias to the north. Above 95 and 30-50. It is noticeable that for IRI, SMR and ACE-FTS the top of the stratospheric ozone layer at mid-latitudes extends to a higher altitude in the summer months, while MIPAS tends to show higher altitudes in spring and autumn. At mid-latitudes, both IRI and SMR consistently depict a stronger secondary maximum in summer and deeper trough in winter, km, the same can be seen in MIPAS even though it is less pronounced. MIPAS observations of ozone density show relatively small temporal and spatial variation. These differences may be relative differences are amplified due to the very low ozone densities and low sensitivity of the instruments, which is noted by the sensitivity analyses in Mlynarczyk and Olander (1995) and Yankovsky et al. (2016).

The uncertainties in the photochemical kinetic and spectroscopic rate coefficients, as well as the lack of in-flight absolute calibration may be main reason for the general positive bias being observed, as listed in Table 1. In addition, as discussed in

Zhu et al. (2007), the result of the lower vertical resolution of MIPAS. ACE-FTS samples ozone profiles at a much lower rate that is not sufficient to produce a continuous time series, thus we show a discrete 2D plot instead of contour plot in Fig. 12. A stronger seasonal variation in influence of transport e.g. tidal motions is non-negligible above 90 km as their amplitudes are large, which may lead to a significant error. Also, they point out that at around 80 km where $O_2(a^1\Delta_g)$ concentration is at its minimum and has high vertical gradient, the mid-latitude bands is also observed by ACE-FTS, with a deeper trough at the end of spring and beginning of autumn. Unlike the others, the spatial and temporal variation of the secondary maximum is not so obvious for ACE-FTS due to the low sampling rate. Overall, IRI agrees very well with SMR, and transport term in the continuity equation become important, to a lesser extent, with MIPAS. All of the instruments display a somewhat weaker secondary maximum in the equatorial region than in mid-latitude regions, which is also shown by Smith et al. (2013) in their Fig. 13.

The differences neglected in our Eq. 17. The abundance of the coincident measurements between IRI, ACE-FTS and MIPAS in Fig. 12 may be explained by their sampling at different SZA and the underlying assumptions in their retrieval techniques. IRI and SMR sample at the same SZA all the time, with lower SZA SMR and OS provides a unique opportunity for a future investigation about the accuracy of the photochemical model. The absolute calibration error can be investigated after a more statistically significant amount of data will be processed (e.g. 19-year data). López-Puertas et al. (2018) have reported that, in the summer months in the mid-latitude belts and rather constant SZA in the equatorial belt. In general MIPAS samples at a lower SZA than IRI and SMR, which will affect the represented mean in the MLT region where the diurnal variation is strong. Regardless of the location and season, ACE-FTS is always sampling at SZA of 90, MIPAS ozone has a negative bias of 20 to 80% between 60 to 85 km, when ozone density experiences a rapid change in the MLT region. Thus such a monthly mean profile should be treated with caution since it may not necessarily well represent the spatial and temporal distribution of daytime ozone km compared to SABER and ACE-FTS, and a positive bias of 10 to 20 % compared to MLS and SMILES (see their Fig. 7c). Investigating the influences of the local time sampling patterns and transport would require a comprehensive modelling study, as well as the processing of a significantly bigger sample of the IRI data set allowing us to look for consistency and separate the different effects that contribute to the error.

Monthly mean ozone number density from November 2007 to October 2008, in three latitude bands: 30-50 (first row), 10-10 (second row) and 30-50 (third row). Columns from the left to right represent IRI, SMR, ACE-FTS and MIPAS, respectively.

4 Conclusions

In this study, we present a presented a technique to retrieve a new high along-track resolution IRA band and ozone dataset. We first briefly presented the updated calibration scheme that is used on the OSIRIS IR imager level 1 data. From Then, from the limb radiance measurements, an the optimal estimation method is used to retrieve the volume emission rate of $O_2(a^1\Delta_g)$ image by image. The implementation of the inversion includes a simple linear forward model that only considers emission in the radiative transfer equation. An example orbit of the linearised scheme with a correction factor to account for the absorption process. The observed dayglow volume emission rate shows features such as a clear a clear structure of a main

layer and a secondary maximum, ~~accompanied by some finer structures. The~~ as well as finer structures along the orbit track.

655 ~~However, the~~ nodding motion of the satellite occasionally 'creates' leads to data gaps through the airglow layers.

~~Once the~~ From the retrieved volume emission rate of $O_2(a^1\Delta_g)$ ~~is retrieved~~, ozone is derived based on the non-linear inversion of a photochemical kinetic model that describes the relationship between ozone and $O_2(a^1\Delta_g)$. The kinetic model is a slightly extended version of the one developed by Mlynczak et al. (1993), which includes mechanisms such as photodissociation of O_2 and O_3 , solar excitation of O_2 and quenching of different excited states of atomic and molecular oxygen.

660 ~~The inversion is-~~

~~However, the validity of the photochemical equilibrium assumption, which is essential when using the kinetic model to retrieve ozone, is questionable for a large portion of the IRI measurements that are located near the night-day terminator, especially near the equator above 75 km. To manage this issue we apply a novel approach where we integrate the uncertainty caused by this effect directly into the retrieval by increasing the measurement uncertainty according to how much the measurement~~

665 ~~conditions diverge from the equilibrium level. This equilibrium index is assessed based on the implementation of the Levenberg-Marquardt algorithm~~ time after local sunrise and the total lifetime of $O_2(a^1\Delta_g)$ as a function of altitude. As a result of such a modification on the measurement uncertainty, the regions where the equilibrium assumption is far from valid are associated with low measurement response and high estimated error, and are thus screened out for further analysis, while other regions remain sensitive to the measurement.

670 Finally, the daytime ozone density retrieved from a test sample of IRI measurements made between November 2007 and October 2008 is compared to ~~the~~ ozone products collected from external instruments, namely SMR, OS ~~, MIPAS and ACE-FTS and MIPAS~~. The comparison of the coincident profiles of IRI, OS and SMR ~~of corresponding to~~ an arbitrarily selected orbit ~~showed~~ shows that they merge rather well, although they do not measure over the same altitude ranges. The comparison also demonstrates the advantage of the high sampling rate of IRI. Zonally averaged monthly mean profiles give us an overall image of

675 ~~the inferred global distribution of ozone. It can be seen that the ozone trough in the MLT is deeper and at lower altitude in the winter hemisphere which is consistent between IRI, SMR, and MIPAS. One year of monthly mean profiles separated into three latitudinal bands depict a clear seasonal pattern in IRI and SMR, with a stronger secondary maximum in the summer months and deeper ozone trough in the winter months especially at mid-latitudes. MIPAS monthly mean ozone also shows a similar annual cycle, but less pronounced. A possible explanation of differences between instruments may come from~~

680 ~~the sampling pattern of the local sun zenith angle and the underlying assumptions in their ozone retrievals such as vertical resolution~~ IRI ozone data set is capable of reproducing the general seasonal and latitudinal distributions in the mesosphere - lower thermosphere, as it is shown in MIPAS and SMR in the same year. The relative difference between IRI and other instruments shows that IRI has a positive bias of up to 25% below 75 km, and up to 50% in some regions above. We believe that this bias mostly comes from the uncertainty in the photochemical model and the absolute calibration process of the limb

685 ~~radiance data but some may still be due to differences in the exact solar illumination conditions of the observations.~~

Overall, this study has demonstrated the technique of retrieving ozone density from the $O_2(a^1\Delta_g)$ limb radiance measurements ~~by IRI from the IR imager on board the Odin satellite~~. The inter-comparisons with ~~the other independent ozone datasets~~

[independent ozone data sets](#) shows that such a technique can be further applied to all IRI limb radiance data throughout the 19 years of the mission to date, leading to a new, long-term, high resolution ozone ~~dataset~~ [data set](#) in the middle atmosphere.

690 *Data availability.* The data will be available on our ftp server [odin-osiris.usask.ca](ftp://odin-osiris.usask.ca) on special request. More information is available at <https://research-groups.usask.ca/osiris/>

Appendix A: Appended tables

Table A1. Reactions and their coefficients included in the photochemical model

Symbol in Fig.5	Reaction	Rate coefficient (in molecule cm s units)	Efficiency	Reference
J _H	$O_3 + h\nu \rightarrow O_2(a^1\Delta_g) + O(^1D)$	Vertical profile	0.9	JPL
J _{src}	$O_2 + h\nu \rightarrow O(^3P) + O(^1D)$	Vertical profile		JPL
J _{Lα}	$O_2 + h\nu \rightarrow O(^3P) + O(^1D)$	Vertical profile	0.44	JPL
g _A	$O_2 + h\nu \rightarrow O_2(b^1\Sigma_g^+, v=0)$	Vertical profile		HITRAN
g _B	$O_2 + h\nu \rightarrow O_2(b^1\Sigma_g^+, v=1)$	Vertical profile		HITRAN
g _{IRA}	$O_2 + h\nu \rightarrow O_2(a^1\Delta_g)$	Vertical profile		HITRAN
A ₁	$O(^1D) \rightarrow O + h\nu(\lambda=630\text{nm})$	6.81×10^{-3}		a
A ₂	$O_2(b^1\Sigma_g^+, v=0) \rightarrow O_2 + h\nu(\lambda=762\text{nm})$	8.34×10^{-2}		a
A ₃	$O_2(b^1\Sigma_g^+, v=1) \rightarrow O_2(b^1\Sigma_g^+, v=1) + h\nu(\lambda=771\text{nm})$	7.2×10^{-2}		a
A ₄	$O_2(a^1\Delta_g) \rightarrow O_2 + h\nu(\lambda=1.24\mu\text{m})$	2.26×10^{-4}		a
Q ₁	$O(^1D) + N_2 \rightarrow O(^3P) + N_2$	$2.15 \times 10^{-11} \times \exp(-110/T)$		JPL
Q _{1a}	$O(^1D) + O_2 \rightarrow O(^3P) + O_2(b^1\Sigma_g^+, v=1)$	$3.3 \times 10^{-11} \times \exp(-55/T)$	0.8	JPL, a
Q _{1b}	$O(^1D) + O_2 \rightarrow O(^3P) + O_2(b^1\Sigma_g^+, v=0)$	$3.3 \times 10^{-11} \times \exp(-55/T)$	0.2	JPL, a
Q _{2a}	$O_2(b^1\Sigma_g^+, v=1) + O_2$ $\rightarrow O_2(X^3\Sigma_g^-, v=1) + O_2(b^1\Sigma_g^+, v=0)$	$2.2 \times 10^{-11} \times \exp(-115/T)$		a
Q _{2a}	$O_2(b^1\Sigma_g^+, v=1) + O(^3P) \rightarrow O_2 + O(^3P)$	4.5×10^{-12}		a
Q _{2a}	$O_2(b^1\Sigma_g^+, v=1) + O_3 \rightarrow 2O_2 + O(^3P)$	3×10^{-10}		a
Q _{2a}	$O_2(b^1\Sigma_g^+, v=1) + N_2 \rightarrow N_2 + O_2(b^1\Sigma_g^+, v=0)$	7×10^{-13}		a
Q _{2b}	$O_2(b^1\Sigma_g^+, v=0) + N_2 \rightarrow O_2(a^1\Delta_g) + N_2$	2.1×10^{-15}		JPL
Q _{2b}	$O_2(b^1\Sigma_g^+, v=0) + O_2 \rightarrow O_2(a^1\Delta_g) + O_2$	3.9×10^{-17}		JPL
Q _{2b}	$O_2(b^1\Sigma_g^+, v=0) + O \rightarrow O_2(a^1\Delta_g) + O$	8×10^{-14}		JPL
Q _{2b}	$O_2(b^1\Sigma_g^+, v=0) + O_3 \rightarrow O_2(a^1\Delta_g) + O_3$	2.2×10^{-11}		JPL
Q _{2b}	$O_2(b^1\Sigma_g^+, v=0) + CO_2 \rightarrow O_2(a^1\Delta_g) + CO_2$	4.2×10^{-13}		JPL
Q ₃	$O_2(a^1\Delta_g) + O_2 \rightarrow 2O_2$	$3.6 \times 10^{-18} \times \exp(-220/T)$		JPL
Q ₃	$O_2(a^1\Delta_g) + N_2 \rightarrow O_2 + N_2$	1×10^{-20}		JPL
Q ₃	$O_2(a^1\Delta_g) + O \rightarrow O_2 + O$	2×10^{-16}		JPL
Q ₃	$O_2(a^1\Delta_g) + O_3 \rightarrow O_2 + O_3$	$5.2 \times 10^{-11} \times \exp(2840/T)$		JPL
Barth	$2O + M \rightarrow O_2^* + M$	$4.7 \times 10^{-33} \times \exp(300/T)$	see footnote	b
Barth	$O_2^* + O, O_2, N_2 \rightarrow \text{all products}$	see footnote		b
Barth	$O_2^* + O_2 \rightarrow O_2 + O_2(b^1\Sigma_g^+)$	see footnote	see footnote	b

a: See reference list in Yankovsky et al. (2016)

b: Empirical quenching coefficients are introduced. In accordance with notation in McDade et al. (1986), $C^{O_2} = 6.6$, $C^O = 19$

JPL: See reference list in the JPL Publication 10-10 (Burkholder et al., 2015)

HITRAN: Gordon et al. (2017)

Table A2. A list of acronyms that ~~has~~have been used in the paper

Acronym	Full spelling
HALOE	Halogen Occultation Experiment
ACE-FTS	atmospheric Chemistry Experiment - Fourier Transform Spectrometer
SOFIE	Solar Occultation for Ice Experiment
GOMOS	Global Ozone Monitoring by Occultation of Stars
SABER	Sounding of the Atmosphere using Broadband Emission Radiometry
MIPAS	Michelson Interferometer for Passive Atmospheric Sounding
SMR	Sub-Millimetre Radiometer
SME	Solar Mesosphere Explorer
SCIAMACHY	SCanning Imaging Absorption SpectroMeter for Atmospheric CHartography
OS	Optical Spectrograph
IRI	Infrared Imager
OSIRIS	Optical Spectrograph and InfraRed Imaging System
METEORS	Mesosphere-Thermosphere Emissions for Ozone Remote Sensing
MLT	Mesosphere and lower thermosphere
OEM	Optimal estimation method
MAP	Maximum a posteriori
AVK	Averaging kernel
MR	Measurement response
FWHM	Full Width Half Maximum
SZA	Solar zenith angle
CMAM	Canadian Middle Atmosphere Model
MSIS	Mass Spectrometer Incoherent Scatter
ECMWF	European Centre for Medium-Range Weather Forecasts
VMR	Volume mixing ratio
IRA band	InfraRed Atmospheric band
A band	Atmospheric band

Author contributions. The main author has prepared all the calculations and figures, the University of Saskatchewan authors have produced the calibrated IRI data and written Sect. 2.1. All authors have contributed to the discussions.

695 *Competing interests.* The authors declare that they have no competing interests.

Acknowledgements. We are thankful to the other instrument teams for access to their datasets. The Atmospheric Chemistry Experiment (ACE), also known as SCISAT, is a Canadian-led mission mainly supported by the Canadian Space Agency. Odin is a Swedish-led satellite project funded jointly by the Swedish National Space Agency (SNSA), the Canadian Space Agency (CSA), the National Technology Agency of Finland (Tekes), and the Centre National d'Etudes Spatiales (CNES) in France. Odin is also part of the ESA's third party mission programme. We also thank ESA and IMK for access to the MIPAS dataset.

References

- Allen, M., Lunine, J. I., and Yung, Y. L.: The Vertical Distribution of Ozone in the Mesosphere and Lower Thermosphere, Tech. Rep. D3, 1984.
- Baron, P., Ricaud, P., Noë, J. d. I., Eriksson, J. E. P., Merino, F., Ridal, M., and Murtagh, D. P.: Studies for the Odin sub-millimetre radiometer. II. Retrieval methodology, *Canadian Journal of Physics*, 80, 341–356, <https://doi.org/10.1139/p01-150>, <https://doi.org/10.1139/p01-150>, 2002.
- Bernath, P. F., McElroy, C. T., Abrams, M. C., Boone, C. D., Butler, M., Camy-Peyret, C., Carleer, M., Clerbaux, C., Coheur, P. F., Colin, R., DeCola, P., DeMazière, M., Drummond, J. R., Dufour, D., Evans, W. F., Fast, H., Fussen, D., Gilbert, K., Jennings, D. E., Llewellyn, E. J., Lowe, R. P., Mahieu, E., McConnell, J. C., McHugh, M., McLeod, S. D., Michaud, R., Midwinter, C., Nassar, R., Nichitiu, F., Nowlan, C., Rinsland, C. P., Rochon, Y. J., Rowlands, N., Semeniuk, K., Simon, P., Skelton, R., Sloan, J. J., Soucy, M. A., Strong, K., Tremblay, P., Turnbull, D., Walker, K. A., Walkty, I., Wardle, D. A., Wehrle, V., Zander, R., and Zou, J.: Atmospheric chemistry experiment (ACE): Mission overview, <https://doi.org/10.1029/2005GL022386>, 2005.
- Boone, C. D., Nassar, R., Walker, K. A., Rochon, Y., McLeod, S. D., Rinsland, C. P., and Bernath, P. F.: Retrievals for the atmospheric chemistry experiment Fourier-transform spectrometer, Tech. rep., 2005.
- Bourassa, A.: The characterization and calibration of the OSIRIS infrared imager, Master's thesis, 2003.
- Bourassa, A. E., Roth, C. Z., Zawada, D. J., Rieger, L. A., McLinden, C. A., and Degenstein, D. A.: Drift-corrected Odin-OSIRIS ozone product: Algorithm and updated stratospheric ozone trends, *Atmospheric Measurement Techniques*, 11, 489–498, <https://doi.org/10.5194/amt-11-489-2018>, 2018.
- Brasseur, G. and Solomon, S.: *Aeronomy of the Middle Atmosphere*, vol. 53, <https://doi.org/10.1017/CBO9781107415324.004>, 2005.
- Burkholder, J. B., Sander, S. P., Abbatt, J. P. D., Barker, J. R., Huie, R. E., Kolb, C. E., Kurylo, M. J., Orkin, V. L., Wilmouth, D. M., and Wine, P. H.: *Chemical Kinetics and Photochemical Data for Use in Atmospheric Studies Evaluation Number 18 NASA Panel for Data Evaluation*, Tech. rep., <http://jpldataeval.jpl.nasa.gov/>, 2015.
- Chapman, S.: On ozone and atomic oxygen in the upper atmosphere, *Philosophical Magazine and Journal of Science*, 10, 369–383, <https://doi.org/10.1080/14786443009461588>, 1930.
- Degenstein, D.: Atmospheric volume emission tomography from a satellite platform, Ph.D. thesis, Saskatoon, 1999.
- Degenstein, D. A., Llewellyn, E. J., and Lloyd, N. D.: Tomographic retrieval of the oxygen infrared atmospheric band with the OSIRIS infrared imager, *Canadian Journal of Physics*, 82, 501–515, <https://doi.org/10.1139/p04-024>, 2004.
- Degenstein, D. A., Gattinger, R. L., Lloyd, N. D., Bourassa, A. E., Wiensz, J. T., and Llewellyn, E. J.: Observations of an extended mesospheric tertiary ozone peak, *Journal of Atmospheric and Solar-Terrestrial Physics*, 67, 1395–1402, <https://doi.org/10.1016/j.jastp.2005.06.019>, 2005a.
- Degenstein, D. A., Lloyd, N. D., Bourassa, A. E., Gattinger, R. L., and Llewellyn, E. J.: Observations of mesospheric ozone depletion during the October 28, 2003 solar proton event OSIRIS, *Geophysical Research Letters*, 32, 1–4, <https://doi.org/10.1029/2004GL021521>, 2005b.
- Degenstein, D. A., Bourassa, A. E., Roth, C. Z., and Llewellyn, E. J.: Limb scatter ozone retrieval from 10 to 60 km using a multiplicative algebraic reconstruction technique, Tech. rep., www.atmos-chem-phys.net/9/6521/2009/, 2009.
- Eriksson, P.: Algorithm Theoretical Basis Document-Level 2 processing, Tech. rep., https://odin.rss.chalmers.se/static/documents/L1_ATBD.pdf, 2017.

- Gordon, I. E., Rothman, L. S., Hill, C., Kochanov, R. V., Tan, Y., Bernath, P. F., Birk, M., Boudon, V., Campargue, A., Chance, K. V., Drouin, B. J., Flaud, J. M., Gamache, R. R., Hodges, J. T., Jacquemart, D., Perevalov, V. I., Perrin, A., Shine, K. P., Smith, M. A., Tennyson, J., Toon, G. C., Tran, H., Tyuterev, V. G., Barbe, A., Császár, A. G., Devi, V. M., Furtenbacher, T., Harrison, J. J., Hartmann, J. M., Jolly, A., Johnson, T. J., Karman, T., Kleiner, I., Kyuberis, A. A., Loos, J., Lyulin, O. M., Massie, S. T., Mikhailenko, S. N., Moazzen-Ahmadi, N., Müller, H. S., Naumenko, O. V., Nikitin, A. V., Polyansky, O. L., Rey, M., Rotger, M., Sharpe, S. W., Sung, K., Starikova, E., Tashkun, S. A., Auwera, J. V., Wagner, G., Wilzewski, J., Wcisło, P., Yu, S., and Zak, E. J.: The HITRAN2016 molecular spectroscopic database, *Journal of Quantitative Spectroscopy and Radiative Transfer*, 203, 3–69, <https://doi.org/10.1016/j.jqsrt.2017.06.038>, 2017.
- 740 Hartogh, P., Jarchow, C., Sonnemann, G. R., and Grygalashvyly, M.: On the spatiotemporal behavior of ozone within the upper mesosphere/mesopause region under nearly polar night conditions, *Journal of Geophysical Research Atmospheres*, 109, <https://doi.org/10.1029/2004JD004576>, 2004.
- 745 Hays, P. B. and Roble, R. G.: Observation of mesospheric ozone at low latitudes, *Planetary and Space Science*, 21, 273–279, [https://doi.org/https://doi.org/10.1016/0032-0633\(73\)90011-1](https://doi.org/https://doi.org/10.1016/0032-0633(73)90011-1), 1973.
- Hoffmann, C. G., Raffalski, U., Palm, M., Funke, B., Golchert, S. H., Hochschild, G., and Notholt, J.: Observation of strato-mesospheric CO above Kiruna with ground-based microwave radiometry - Retrieval and satellite comparison, *Atmospheric Measurement Techniques*, 4, 2389–2408, <https://doi.org/10.5194/amt-4-2389-2011>, 2011.
- 750 Huang, F. T., Mayr, H. G., Russell, J. M., Mlynczak, M. G., and Reber, C. A.: Ozone diurnal variations and mean profiles in the mesosphere, lower thermosphere, and stratosphere, based on measurements from SABER on TIMED, *Journal of Geophysical Research: Space Physics*, 113, <https://doi.org/10.1029/2007JA012739>, 2008.
- 755 Ivanov, E.: Computer Modeling of the OSIRIS Infrared Imager, Master's thesis, University of Saskatchewan, 2000.
- Kyrölä, E., Tamminen, J., Sofieva, V., Bertaux, J. L., Hauchecorne, A., Dalaudier, F., Fussen, D., Vanhellefont, F., Fanton D'Andon, O., Barrot, G., Guirlet, M., Fehr, T., and Saavedra De Miguel, L.: GOMOS O₃, NO₂, and NO₃ observations in 2002–2008, *Atmospheric Chemistry and Physics*, 10, 7723–7738, <https://doi.org/10.5194/acp-10-7723-2010>, 2010.
- Llewellyn, E. J., Lloyd, N. D., Degenstein, D. A., Gattinger, R. L., Petelina, S. V., Bourassa, A. E., Wiensz, J. T., Ivanov, E. V., McDade, I. C., Solheim, B. H., McConnell, J. C., Haley, C. S., von Savigny, C., Sioris, C. E., McLinden, C. A., Griffioen, E., Kaminski, J., Evans, W. F. J., Puckrin, E., Strong, K., Wehrle, V., Hum, R. H., Kendall, D. J. W., Matsushita, J., Murtagh, D. P., Brohede, S., Stegman, J., Witt, G., Barnes, G., Payne, W. F., Piché, L., Smith, K., Warshaw, G., Deslauniers, D. L., Marchand, P., Richardson, E. H., King, R. A., Wevers, I., McCreath, W., Kyrölä, E., Oikarinen, L., Leppelmeier, G. W., Auvinen, H., Mégie, G., Hauchecorne, A., Lefèvre, F., de La Nöe, J., Ricaud, P., Frisk, U., Sjöberg, F., von Schéele, F., and Nordh, L.: The OSIRIS instrument on the Odin spacecraft, *Canadian Journal of*
- 760 *Physics*, 82, 411–422, <https://doi.org/10.1139/p04-005>, <https://doi.org/10.1139/p04-005>, 2004.
- 765 López-Puertas, M., García-Comas, M., Funke, B., Gardini, A., Stiller, G. P., Von Clarmann, T., Glatthor, N., Laeng, A., Kaufmann, M., Sofieva, V. F., Froidevaux, L., Walker, K. A., and Shiotani, M.: MIPAS observations of ozone in the middle atmosphere, *Atmospheric Measurement Techniques*, 11, 2187–2212, <https://doi.org/10.5194/amt-11-2187-2018>, 2018.
- Marsh, D., Smith, A., Brasseur, G., Kaufmann, M., and Grossmann, K.: The existence of a tertiary ozone maximum in the high-latitude middle mesosphere, *Geophysical Research Letters*, 28, 4531–4534, <https://doi.org/10.1029/2001GL013791>, 2001.
- 770 McDade, I., Murtagh, D., Greer, R., Dickinson, P., Witt, G., Stegman, J., Llewellyn, E., Thomas, L., and Jenkins, D.: ETON 2: Quenching parameters for the proposed precursors of O₂(b¹Σ_g⁺) and O(1S) in the terrestrial nightglow, *Planetary and Space Science*, 34, 789–800, [https://doi.org/10.1016/0032-0633\(86\)90075-9](https://doi.org/10.1016/0032-0633(86)90075-9), 1986.

- McLinden, C. A., Fioletov, V. E., Haley, C. S., Lloyd, N., Roth, C., Degenstein, D., Bourassa, A., McElroy, C. T., and Llewellyn, E. J.: An
775 evaluation of Odin/OSIRIS limb pointing and stratospheric ozone through comparisons with ozonesondes, *Canadian Journal of Physics*,
85, 1125+, 2007.
- Mlynczak, M. G. and Olander, D. S.: On the utility of the molecular oxygen dayglow emissions as proxies for middle atmospheric ozone,
Tech. Rep. 11, 1995.
- Mlynczak, M. G., Solomon, S., and Zaras, D. S.: An updated model for O₂(a¹Δ_g) concentrations in the mesosphere and lower thermo-
780 sphere and implications for remote sensing of ozone at 1.27 μm, *Journal of Geophysical Research: Atmospheres*, 98, 18 639–18 648,
<https://doi.org/10.1029/93JD01478>, 1993.
- Mlynczak, M. G., Morgan, F., Yee, J. H., Espy, P., Murtagh, D., Marshall, B., and Schmidlin, F.: Simultaneous measurements
of the O₂(1Δ) and O₂(1Σ) airglows and ozone in the daytime mesosphere, *Geophysical Research Letters*, 28, 999–1002,
<https://doi.org/10.1029/2000GL012423>, 2001.
- 785 Mlynczak, M. G., Marshall, B. T., Martin-Torres, F. J., Russell, J. M., Thompson, R. E., Remsberg, E. E., and Gordley, L. L.: Sound-
ing of the Atmosphere using Broadband Emission Radiometry observations of daytime mesospheric O₂ (1Δ) 1.27 μm emission and
derivation of ozone, atomic oxygen, and solar and chemical energy deposition rates, *Journal of Geophysical Research Atmospheres*, 112,
<https://doi.org/10.1029/2006JD008355>, 2007.
- Murtagh, D., Frisk, U., Merino, F., Ridal, M., Jonsson, A., Stegman, J., Witt, G., Eriksson, P., Jiménez, C., Megie, G., De la Noë, J., Ricaud,
790 P., Baron, P., Pardo, J. R., Hauchcorne, A., Llewellyn, E. J., Degenstein, D. A., Gattinger, R. L., Lloyd, N. D., Evans, W. F., McDade,
I. C., Haley, C. S., Sioris, C., Von Savigny, C., Solheim, B. H., McConnell, J. C., Strong, K., Richardson, E. H., Leppelmeier, G. W.,
Kyrölä, E., Auvinen, H., and Oikarinen, L.: An overview of the Odin atmospheric mission, *Canadian Journal of Physics*, 80, 309–319,
<https://doi.org/10.1139/P01-157>, 2002.
- Murtagh, D., Skyman, A., Rydberg, B., and Eriksson, P.: Odin/SMR Diagnostic Dataset: Technical Note, Tech. rep., [https://odin.rss.chalmers.
795 se/static/documents/DDS.pdf](https://odin.rss.chalmers.se/static/documents/DDS.pdf), 2018.
- Newman, S. M., Orr-Ewing, A. J., Newnham, D. A., and Ballard, J.: Temperature and pressure dependence of line widths and
integrated absorption intensities for the O₂ a¹g - X³g⁻ (0,0) transition, *Journal of Physical Chemistry A*, 104, 9467–9480,
<https://doi.org/10.1021/jp001640r>, 2000.
- Picone, J. M., Hedin, A. E., Drob, D. P., and Aikin, A. C.: NRLMSISE-00 empirical model of the atmosphere: Statistical comparisons and
800 scientific issues, *Journal of Geophysical Research: Space Physics*, 107, <https://doi.org/10.1029/2002JA009430>, 2002.
- R. J. Thomas, C. A. Barth, G. J. Rottman, D. W. Rusch, G. H. Mount, G. M. Lawrence, R. W. Sanders, G. E. Thomas, and L. E. Clemens:
Ozone density distribution in the mesosphere (50-90 km) measured by the SME limb scanning near infrared spectrometer, *Geophysical
Research Letters*, <https://doi.org/10.1029/gl010i004p00245>, 1983.
- Rodgers, C. D.: Inverse methods for atmospheric sounding : theory and practice., Series on atmospheric, oceanic and
805 planetary physics: 2, World Scientific, [http://search.ebscohost.com/login.aspx?direct=true&AuthType=sso&db=cat07470a&AN=clc.
8b34e549d2e147e7ad113df41218f018&site=eds-live&scope=site&custid=s3911979&authtype=sso&group=main&profile=eds](http://search.ebscohost.com/login.aspx?direct=true&AuthType=sso&db=cat07470a&AN=clc.8b34e549d2e147e7ad113df41218f018&site=eds-live&scope=site&custid=s3911979&authtype=sso&group=main&profile=eds), 2000.
- Sheese, P.: Mesospheric ozone densities retrieved from OSIRIS observations of the O₂ A-band dayglow, Ph.D. thesis, 2009.
- Smith, A. K., Harvey, V. L., Mlynczak, M. G., Funke, B., García-Comas, M., Hervig, M., Kaufmann, M., Kyrölä, E., López-Puertas, M.,
McDade, I., Randall, C. E., Russell, J. M., Sheese, P. E., Shiotani, M., Skinner, W. R., Suzuki, M., and Walker, K. A.: Satellite observations
810 of ozone in the upper mesosphere, *Journal of Geophysical Research Atmospheres*, 118, 5803–5821, <https://doi.org/10.1002/jgrd.50445>,
2013.

- Smith, A. K., Espy, P. J., López-Puertas, M., and Tweedy, O. V.: Spatial and Temporal Structure of the Tertiary Ozone Maximum in the Polar Winter Mesosphere, *Journal of Geophysical Research: Atmospheres*, 123, 4373–4389, <https://doi.org/10.1029/2017JD028030>, 2018.
- 815 Sofieva, V. F., Rahpoe, N., Tamminen, J., Kyrölä, E., Kalakoski, N., Weber, M., Rozanov, A., Von Savigny, C., Laeng, A., Von Clarmann, T., Stiller, G., Lossow, S., Degenstein, D., Bourassa, A., Adams, C., Roth, C., Lloyd, N., Bernath, P., Hargreaves, R. J., Urban, J., Murtagh, D., Hauchecorne, A., Dalaudier, F., Van Roozendaal, M., Kalb, N., and Zehner, C.: Harmonized dataset of ozone profiles from satellite limb and occultation measurements, *Earth System Science Data*, 5, 349–363, <https://doi.org/10.5194/essd-5-349-2013>, 2013.
- Sofieva, V. F., Kalakoski, N., Päivärinta, S. M., Tamminen, J., Laine, M., and Froidevaux, L.: On sampling uncertainty of satellite ozone profile measurements, *Atmospheric Measurement Techniques*, 7, 1891–1900, <https://doi.org/10.5194/amt-7-1891-2014>, 2014.
- 820 Thomas, R. J., Barth, C. A., Rusch, D. W., and Sanders, R. W.: Solar Mesosphere Explorer near-infrared spectrometer: measurements of 1.27 micrometer radiances and the inference of mesospheric ozone., *Journal of Geophysical Research*, <https://doi.org/10.1029/JD089iD06p09569>, 1984.
- Van der A, R., Adams, C., Bernath, P., Von Clarmann, T., Coldewey-Egbers, M., Degenstein, D., Dudhia, A., Hargreaves, R., Laeng, A., Lerot, C., Loyola, D., Van Peet, J., Rahpoe, N., Sofieva, V., Stiller, G., Tamminen, J., Urban, J., Roozendaal, M. V., Weber, M., Lerot, C., 825 Danckaert, T., Astoreca, R., Heue, K.-P., Sheese, P., Walker, K., and Tukiainen, S.: Ozone CCI Algorithm Theoretical Basis Document Phase 2 Version 2 (ATBDv2), Tech. rep., http://cci.esa.int/sites/default/files/filedepot/incoming/Ozone_cci_ATBD_Phase2_V2.pdf, 2017.
- Yankovsky, V. A. and Manuilova, R. O.: Model of daytime emissions of electronically-vibrationally excited products of O₃ and O₂ photolysis: application to ozone retrieval, *Annales Geophysicae*, 24, 2823–2839, <https://doi.org/10.5194/angeo-24-2823-2006>, <https://www.ann-geophys.net/24/2823/2006/>, 2006.
- 830 Yankovsky, V. A., Martyshenko, K. V., Manuilova, R. O., and Feofilov, A. G.: Oxygen dayglow emissions as proxies for atomic oxygen and ozone in the mesosphere and lower thermosphere, *Journal of Molecular Spectroscopy*, 327, 209–231, <https://doi.org/10.1016/j.jms.2016.03.006>, 2016.
- Zarboo, A., Bender, S., Burrows, J. P., Orphal, J., and Sinnhuber, M.: Retrieval of O₂(1Σ) and O₂(1Δ) volume emission rates in the mesosphere and lower thermosphere using SCIAMACHY MLT limb scans, *Atmospheric Measurement Techniques*, 11, 473–487, 835 <https://doi.org/10.5194/amt-11-473-2018>, 2018.
- Zhu, X., Yee, J. H., and Talaat, E. R.: Effect of dynamical-photochemical coupling on oxygen airglow emission and implications for daytime ozone retrieved from 1.27 μm emission, *Journal of Geophysical Research Atmospheres*, 112, <https://doi.org/10.1029/2007JD008447>, 2007.